Astronomy & Astrophysics

MIRI Deep Imaging Survey (MIDIS) of the Hubble Ultra Deep Field

Survey description and early results for the galaxy population detected at 5.6 μm[*]

Göran Östlin[1,**][ORCID], Pablo G. Pérez-González[2][ORCID], Jens Melinder[1][ORCID], Steven Gillman[3,6][ORCID], Edoardo Iani[4,29],
Luca Costantin[2][ORCID], Leindert A. Boogaard[20,5][ORCID], Pierluigi Rinaldi[27,4], Luis Colina[2][ORCID], Hans Ulrik Nørgaard-Nielsen[3,†],
Daniel Dicken[7][ORCID], Thomas R. Greve[3,6,8], Gillian Wright[7], Almudena Alonso-Herrero[25][ORCID], Javier Álvarez-Márquez[2][ORCID],
Marianna Annunziatella[2], Arjan Bik[1][ORCID], Sarah E. I. Bosman[5,9], Karina I. Caputi[4,6], Alejandro Crespo Gomez[2][ORCID],
Andreas Eckart[10,30], Macarena Garcia-Marin[11], Jens Hjorth[12], Olivier Ilbert[13], Iris Jermann[3,6][ORCID],
Sarah Kendrew[11][ORCID], Alvaro Labiano[25,26], Danial Langeroodi[12][ORCID], Olivier Le Fevre[13,†], Mattia Libralato[14,28],
Romain A. Meyer[15,5][ORCID], Thibaud Moutard[16][ORCID], Florian Peissker[10], John P. Pye[17][ORCID], Tuomo V. Tikkanen[17][ORCID],
Martin Topinka[18][ORCID], Fabian Walter[5][ORCID], Martin Ward[19], Paul van der Werf[20], Ewine F. van Dishoeck[20][ORCID],
Manuel Güdel[21,22], Thomas Henning[5], Pierre-Olivier Lagage[23], Tom P. Ray[18][ORCID], and Bart Vandenbussche[24]

(Affiliations can be found after the references)

ABSTRACT

*Context.* The recently launched James Webb Space Telescope (JWST) is opening new observing windows on the distant Universe. Among JWST's instruments, the Mid Infrared Instrument (MIRI) offers the unique capability of imaging observations at wavelengths of $\lambda > 5\,\mu m$. This enables unique access to the rest frame near-infrared (NIR, $\lambda \geq 1\,\mu m$) emission from galaxies at redshifts of $z > 4$ and the visual ($\lambda \gtrsim 5000\,\text{Å}$) rest frame for $z > 9$. We report here on the guaranteed time observations (GTO), from the MIRI European Consortium, of the Hubble Ultra Deep Field (HUDF), forming the MIRI Deep Imaging Survey (MIDIS), consisting of an on source integration time of ~41 hours in the MIRI/F560W (5.6 μm) filter. The F560W filter was selected since it would produce the deepest data in terms of AB magnitudes in a given time. To our knowledge, this constitutes the longest single filter exposure obtained with JWST of an extragalactic field as of yet.
Aims. The HUDF is one of the most observed extragalactic fields, with extensive multi-wavelength coverage, where (before JWST) galaxies up to $z \sim 7$ have been confirmed, and at $z > 10$ suggested, from HST photometry. We aim to characterise the galaxy population in HUDF at 5.6 μm, enabling studies such as: the rest frame NIR morphologies for galaxies at $z \lesssim 4.6$, probing mature stellar populations and emission lines in $z > 6$ sources, intrinsically red and dusty galaxies, and active galactic nuclei (AGNs) and their host galaxies at intermediate redshifts.
Methods. We reduced the MIRI data using the official JWST pipeline, augmented by in-house custom scripts. We measured the noise characteristics of the resulting image. Galaxy photometry was obtained, and photometric redshifts were estimated for sources with available multi-wavelength photometry (and compared to spectroscopic redshifts when available).
Results. Over the deepest part of our image, the 5σ point source limit is 28.65 mag AB (12.6 nJy), ~0.35 mag better than predicted by the JWST exposure time calculator. We find ~2500 sources, the overwhelming majority of which are distant galaxies, but we note that spurious sources likely remain at faint magnitudes due to imperfect cosmic ray rejection in the JWST pipeline. More than 500 galaxies with available spectroscopic redshifts, up to $z \approx 11$, have been identified, the majority of which are at $z < 6$. More than 1000 galaxies have reliable photometric redshift estimates, of which ~25 are at $6 < z < 12$. The point spread function in the F560W filter has a full width at half maximum (FWHM) of $\approx 0.2''$ (corresponding to 1.4 kpc at $z = 4$), allowing the NIR rest frame morphologies and stellar mass distributions to be resolved for $z < 4.5$. Moreover, >100 objects with very red NIRCam vs MIRI (3.6–5.6 μm > 1 mag) colours have been found, suggestive of dusty or old stellar populations at high redshifts.
Conclusions. We conclude that MIDIS surpasses preflight expectations and that deep MIRI imaging has great potential to characterise the galaxy population from cosmic noon to dawn.

Key words. galaxies: evolution – galaxies: formation – galaxies: high-redshift – infrared: galaxies

1. Introduction

The late 1990s marked a revolution in the study of the high-redshift Universe. This was made possible through new facilities such as the Hubble Space Telescope (HST), and 8–10 m class ground-based telescopes such as the Keck and its successors, notably the ESO/VLT. While before, redshifts of $z > 1$ were mostly the domain of quasi-stellar objects (QSOs) and radio galaxies (see Giavalisco 2002, for a review), breakthroughs such as the Lyman break technique (Steidel & Hamilton 1992; Steidel et al. 1996a, implying dropouts in the bluer filters due to a redshifted Lyman break), more sensitive narrow-band surveys for Lyman α (Lyα) emitters (Hu et al. 1998), and not least the advent of the Hubble Deep Field (HDF, Williams et al. 1996) dramatically changed the picture (Steidel et al. 1996b;

Williams 2018). The HDF was an ambitious undertaking by imaging an apparently blank and almost starless field at high Galactic latitude with HST in several filters with exposure times amounting to 30–40 hours per filter in U, B, V, and I. The HDF was found to be anything but blank, containing thousands of distant galaxies, and triggered a wealth of high-z studies (Williams 2018). Spectroscopic campaigns confirmed many galaxies in the HDF to be at high redshifts, and dropout and photometric redshift techniques could show with high probability that many sources too faint for ground-based spectroscopy are likely to reside at very high redshifts (Williams 2018). The HDF was followed over the years by several other deep field campaigns from the ground, and notably with the HST, for instance HDF-south (Williams et al. 2000), GOODS (Great Observatories Origins Deep Survey Giavalisco et al. 2004), and the Hubble Ultra Deep Field (HUDF, Beckwidth et al. 2016), which is contained within the GOODS south (GOODS-S) field. Such deep field studies aim to explore when galaxies formed and how they have evolved over cosmic time.

At redshifts of $z \gtrsim 4$, the absorption by neutral hydrogen in the intergalactic medium (IGM) efficiently suppresses any emission bluewards of Lyα, meaning that the 'dropouts' would mainly trace the Lyα break (1216Å) rather than the Lyman discontinuity (912 Å, Madau 1995; Inoue et al. 2014). With optical-only observations, this originally limited dropout studies with HST to $z < 6$. In 1997, near-infrared (NIR) capability was added to HST with the NICMOS instrument (Near Infrared Camera and Multi Object Spectrometer, Thompson et al. 1999), which had a very small field of view (≤ 0.75 arcmin^2), and led to the discovery of ~20 candidates at $z \gtrsim 7$ from hundreds of orbits of HST imaging (Bouwens et al. 2010). With the advent of HST Wide Field Camera 3 (WFC3, installed during HST servicing mission 4 in 2009), with its NIR channel operating up to 1.7 μm and a much larger field of view and sensitivity compared to NICMOS, the field was revitalised and the redshift frontier pushed to $z \sim 10$ (e.g. Bouwens et al. 2015). In all, several deep and wide observing programmes, such as CANDELS (the Cosmic Assembly Near-IR Deep Extragalactic Legacy Survey, Koekemoer et al. 2011) and the HST Frontier Fields (Lotz et al. 2017), have led to the detection of several hundreds of galaxy candidates at $z > 7$ (Bouwens et al. 2015) and to a better characterisation of the properties of galaxies at $z > 1$. The deepest field observed with HST to date remains the HUDF, of which the fraction with the deepest WFC3/IR observations forms the eXtremely Deep Field (XDF, Illingworth et al. 2013).

At longer wavelengths, significant capability beyond 2.2 μm (the K-band, the reddest filter practically useful for deep ground-based surveys) was added by the Spitzer Space Telescope from 2004 and onwards, though it lacked the spatial resolution of HST (Fazio et al. 2004a), and was therefore susceptible to source confusion at faint fluxes. Notably, the GOODS areas have been extensively imaged with the Infrared Array Camera (IRAC, which has broadband filters centred at 3.6, 4.5, 5.8, and 8 μm) on board Spitzer. The bluest two filters of IRAC (Ch1 and Ch2) were also observed during the extended warm phase of the Spitzer mission, resulting in exposure times of ~200 h in the HUDF, but the two longer wavelength filters (Ch3 and Ch4) were not operating in the warm mission phase. Hence, IRAC imaging of the HUDF is significantly shallower at $\lambda > 5$ μm (Stefanon et al. 2021). The observations presented in this paper (MIRI with filter F560W) have a bandpass similar to IRAC/Ch3, allowing the increase in performance with JWST/MIRI to be quantified.

The quest for the highest-redshift galaxies is ultimately about finding the first galaxies that appeared in the Universe. Following the Big Bang and the subsequent cosmic recombination, the Universe was neutral but with little structure. As density inhomogeneities grew, stars, galaxies and massive black holes eventually formed, and their ionising photon output gradually ionised the IGM (reionisation). Studies of QSO absorption lines (i.e. finding the Gunn-Peterson trough, Gunn & Peterson 1965) indicate that this process was largely complete around $z \sim 6$ (Becker et al. 2001; Fan et al. 2006), but likely extended to $z \sim 5.3$ (Bosman et al. 2022). Redshifts $z \gtrsim 6$ are commonly referred to as the epoch of reionisation (EoR).

Already in the mid 1990s, at the times when HST was delivering its first deep images, the need for a successor operating at infrared (IR) wavelengths was identified, as galaxies at $z > 6$ would become invisible at optical wavelengths. Hence, the Next Generation Space Telescope (NGST) project began to be developed for an IR-optimised observatory, and in 2002, NASA renamed it the James Webb Space Telescope (JWST), which was eventually launched on December 25, 2021.

The JWST (Gardner et al. 2023; Rigby et al. 2023) features four scientific instruments, MIRI, NIRCam, NIRISS and NIRSpec. While the latter three are optimised for imaging and spectroscopy in the NIR, MIRI, the Mid Infrared Instrument (Rieke et al. 2015; Wright et al. 2015) is (as the name implies) optimised for the mid IR (MIR) and uniquely probes the 5–28 μm range in imaging, spectroscopy and coronography.

The launch of JWST, (originally and casually conceived as 'the first light machine') has opened up a new window for the high-z Universe. By extending the red cutoff to much longer wavelengths than HST, higher redshifts can be probed by the imaging dropout technique. NIRCam covers $\lambda \leq 5$ μm with many filters and could in principle detect dropouts to $z \sim 30$ (should such galaxies exist and be bright enough).

However, even for a young galaxy, most of the stellar mass is carried by lower-mass stars whose spectral flux density (f_ν) peaks at rest frame $\lambda_{rest} > 0.5$ μm, which for $z > 9$ is the domain of MIRI. Moreover, as evolved stellar populations have redder colours (and reduced flux at $\lambda < 0.5$ μm) the ability to detect an evolved stellar population underlying a younger one increases with wavelength, and MIRI data is therefore vital for characterising the stellar populations and star formation histories of galaxies at $z > 5$. Moreover, at $z > 6.6$, Hα, the prime probe of star formation activity in galaxies and which is strong in AGN, shifts into the MIRI range, again making it a vital instrument for studying star forming galaxies (e.g. Rinaldi et al. 2023), and supermassive black holes in the EoR (e.g. Bosman et al. 2024).

Longer wavelengths are also less affected by dust extinction, and massive starbursts are known to have large amounts of extinction (both at low and high-z) and the unique ability of MIRI to probe the rest frame NIR ($\lambda > 1$ μm) for $z > 4$, and Paschen α for $z > 2$ offers unique opportunities to probe such galaxies (e.g. GN20, Colina et al. 2023). Many such massive galaxies also contain an AGN whose hot dust torus emission tends to dominate the SED at $\lambda_{rest} > 2$ μm which for $z > 1$ can be uniquely probed by MIRI (Lyu et al. 2022; Perez-Gonzalez et al. 2024a).

Such considerations led the MIRI European Consortium (MIRI-EC) to allocate ~64 hours of their guaranteed time observations (GTO), for deep imaging of the HUDF/XDF with MIRI in filter F560W, forming the MIRI Deep Imaging Survey (MIDIS, programme 1283). The F560W filter was selected because (based on the pre-flight sensitivity estimates) it reached the faintest flux limit in a given time of all the MIRI filters, and

with the intent to seed future GO deep imaging projects of the HUDF with longer wavelength MIRI filters.

Since the commissioning of JWST, a number of studies based on Early Release Observations (ERO), Early Release Science (ERS), GTO, and General Observer (GO) programs have demonstrated the power of JWST to probe galaxies in the EoR. Notable are the results from NIRCam, where ERO/ERS/GTO-based studies provided many candidates with probable redshifts $z > 9$ (see Harikane et al. 2023, 2024; Perez-Gonzalez et al. 2023), and the results from the large GTO programmeJADES (Robertson et al. 2023; Rieke et al. 2023). MIRI was less used in the ERO/ERS programs, but its potential to characterise galaxies in the EoR has been demonstrated (e.g. Papovich et al. 2023). However, the EoR is just the tip of the iceberg, and both NIR-Cam and MIRI can revolutionise the study of vastly more galaxies from cosmic noon ($z \gtrsim 1$) to the EoR, by probing rest-frame optical and NIR emission where HST is severely compromised by its red cutoff at $\lambda \sim 1.7\,\mu m$, and the decommissioned Spitzer/IRAC by its wider point spread function (PSF) and lower sensitivity. This has already been demonstrated in several studies.

In this paper, we present an overview of the MIRI Deep Imaging Survey (MIDIS), a MIRI European Consortium (MIRI-EC) GTO project (programmeID 1283), imaging the HUDF/XDF with MIRI at 5.6 μm, forming the longest exposure of a single extragalactic field with MIRI obtained to date (see Casey et al. 2023). In parallel, deep NIRCam imaging and NIRISS slitless spectroscopy were obtained for two adjacent fields with deep HST coverage. The parallels were chosen to enable selection of: $z > 7$ galaxy candidates through the dropout technique (NIRCam); and $z > 1$ emission line and continuum bright galaxies (NIRISS). The MIDIS project has already resulted in a number of papers and more are in preparation, as described below.

The outline of the paper is as follows: in Section 2 we describe the observations, in Section 3 we describe the reductions and quantify the photometric depth; Section 4 mentions the ancillary data used, Section 5 describes photometric measurements including a comparison with Spitzer, Section 6 describes the photometric redshift estimation, while Section 7 give examples of results from MIDIS, and Section 8 contains a summary and conclusions; at the end we describe how to access the our MIRI F560W images and catalogue.

Throughout the paper, all the magnitudes quoted are in the AB system. We assume a cosmology with $H_0 = 70\,\mathrm{km\,s^{-1}\,Mpc^{-1}}$, $\Omega_m = 0.3$, and $\Omega_\Lambda = 0.7$.

2. Observations

A single pointing coincident on the XDF was selected for imaging in a single MIRI filter, F560W. Parallel observations were defined for about 63% of the time with NIRCam (targeting parallel field P2), and 37% with NIRISS (targeting parallel field P3). Both parallel fields have deep HST imaging (Whitaker et al. 2019). As a special requirement, we requested the observations to be executed under low-background conditions. The MIRI observations were designed to be split up into six observations (or spacecraft visits), four (Obs 1–4) with NIRCam in parallel and two (Obs 5–6) with NIRISS in parallel.

For Obs 1–4, MIRI data acquisition was designed to use the FASTR1 readout mode with 100 groups per integration, 10 integrations per dither position, and 10 dither positions for a total exposure time of 28 000 seconds (28 ks) per observation. For dithering, the CYCLING-MEDIUM pattern was adopted that

provides 0.5 pixel (the MIRI imager pixel scale is 0.11″/pixel) sampling for MIRI imaging. This dithering pattern was selected to provide offsets between exposures that were larger than the anticipated sizes of all but the brightest objects in the field. Observations 1, 2, 3, and 4 (each consisting of 10 positions) were selected to use starting points 1, 11, 21, and 31, respectively, to have each exposure at a different position. In order to further improve the PSF sampling, small (one quarter to one third MIRI pixel) manual offsets were employed at the beginning of each subsequent observation following observation 1 (by using the special requirement OFFSET). All observations were to be obtained at the same position angle (PA). Obs 1–2 would use NIRCam F115W/F277W in parallel and Obs 3–4 NIRCam F150W/F356W.

For Obs 5 and 6, NIRISS was selected as the parallel instrument. During Obs 5 a single 100 group F560W exposure (277.5 s) would be obtained (coincident with a parallel NIRISS F115W direct image) at the nominal position, followed by a 9-point dither (again using CYCLING-MEDIUM) with 100 groups and 4 integrations (10 065 s, when parallel NIRISS slitless spectroscopy with GR150R was to be obtained), and then another single 100 group F560W exposure (again with NIRISS/F115W imaging in parallel). The starting point for the dither pattern was 41. The same sequence was to be repeated (using the same dither positions) with NIRISS/F150W in parallel. Finally, the same sequence would be repeated with NIRISS/F200W in parallel, but here the initial and final F560W image (where direct NIRISS/F200W images were to be obtained) had two integrations per exposure (557.8 s). The direct images were to be obtained with at the nominal position (no dithers). Hence, for each of the nine points in the cycling pattern there would be 12 integrations with 100 groups (a total of 3355 seconds per position), and for the nominal position 8 integrations with 100 groups (total 2225.6 seconds).

For Obs 6, the same parameters were used but here using dithering starting point 50, following a 0.0328 arcsec shift in x and y, again to improve the MIRI sampling, and with the NIRISS spectral observations using the grism with orthogonal dispersion direction (GR150C). Obs 5–6 were to be obtained at the same PA, and with a 5 degree tolerance with respect to Obs 1–4.

The observations were scheduled for early December 2022, and Obs 5–6, and 1–2 were successfully obtained on Dec 2–6. However, repeated JWST safing events prevented a timely execution of Obs 3–4, and as time slipped and the spacecraft V3 angle was evolving, we were forced to revise the PA constraints for Obs 3–4, and we added a small spatial offset to ensure better joint coverage of the NIRCam parallel (using filters F150W and F356W) with Obs 1 and 2 (using filters F115W and F277W). In the end, only Obs 4 could be executed, and Obs 3 was postponed to December 2023. In light of this, it was decided to dedicate the MIRI observing time of Obs 3 to F1000W imaging (with NIRCam F150W + F356W in parallel) at the same pointing and PA as for Obs 1, and observations (now re-labeled as Obs 7) were executed December 6, 2023. These F1000W observations will be presented in a forthcoming paper (Östlin et al., in prep.; see also Perez-Gonzalez et al. 2024b).

Hence, for the MIRI/F560W imaging we obtained 5/6 of the requested observations, at 3 different PAs, and at 50 different dither positions, see Table A.1. The total net exposure time in F560W amounts to 148 842 seconds (41.34 hours). To our knowledge, this made it the longest imaging exposure obtained of a single extragalactic field obtained with JWST at the time. The fact that Obs 4 was offset and rotated with respect to Obs

1–2 means that we cover a larger area, but with less depth particularly in the NE parts.

The footprints of the MIRI primary observations and the parallel NIRCam/NIRISS observations are shown in Fig. 1. The use of different starting positions for the five observations (enabled by the OFFSET special requirement) with non-integer pixel shifts, and the use of 3 different PAs means that the subpixel phase space is quite uniformly populated, see Fig. 2, which is valid near the field centre (further away, the relative positions are modulated by the geometric distortion of the MIRI imager). The total exposure times in the parallel observations are slightly shorter (by 2% for NIRCam, 27 593 s per Obs; and 5% for NIRISS, with 2147 s for imaging and 28 699 s for grism spectroscopy, split over the three settings).

For context and comparison, we show in Fig. 3 the MIDIS F560W footprint (orange shade) compared to the larger area, but shallower (exposure depth ranging from 0.65 ks in F560W to 2.2 ks in F2100W) multi-filter MIRI imaging survey SMILES (programme 1207 Rieke et al. 2024; Alberts et al. 2014) and the borders of the NIRCam primary imaging area of the JADES survey (Rieke et al. 2023; Eisenstein et al. 2023a).

In Fig. 4 we show the resulting image (see Section 3) and exposure map for the mosaic of all F560W observations. Due to the use of different pointings and PAs the mosaic boundary has a complex shape. For convenience in characterising the varying depth over the field of MIDIS, we define regions of approximately equal depth:

- A (deepest, yellow) defined by the overlapping regions of the MIRI imaging field formed by Obs 1–2, 4 and 5–6, where the exposure time is 37–41.3 h.
- B (deep, green) where the exposure time is ≥24 h. This also includes the Lyot region for Obs 1–2 and 5–6 and with partial overlap from Obs 4. The depth in the Lyot region is non-uniform due to the occulting mask and supporting instrument struts.
- C (NE extension, purple) mainly represents the area of Obs 4 which does not have overlapping observations from Obs 1–2, 5–6, and where the total exposure time amounts to ≥7 h.
- In the area outside of these regions (the 'external' region) the depth varies due to partially overlapping dither positions and ranges from ∼1 (very small area) to ∼6 hours.

The NIRCam and NIRISS parallel observations will be described in forthcoming papers. Some results from the NIRCam parallels have already be published (Perez-Gonzalez et al. 2023; Caputi et al. 2024) and more are in preparation.

3. Reductions and calibration

Three different groups within the team made independent reductions to allow for cross-validation of the final images and photometry. The data were first reduced and calibrated with the JWST pipeline. This produced images with residual stripes and residual background (Morrison et al. 2023; Dicken et al. 2006). We adopted different schemes designed to counter these effects while not distorting the photometric calibration (defining our 'customised' pipeline, see below). In addition, we applied an iterative masking of sources for the background estimation: sources appearing after the first run were masked, and then the background was refitted masking new sources that appeared; in total, three passes were done.

After careful vetting of the resulting mosaics from the three groups, they showed a very good overall photometric agreement, and were found to be largely equivalent. We adopted the version
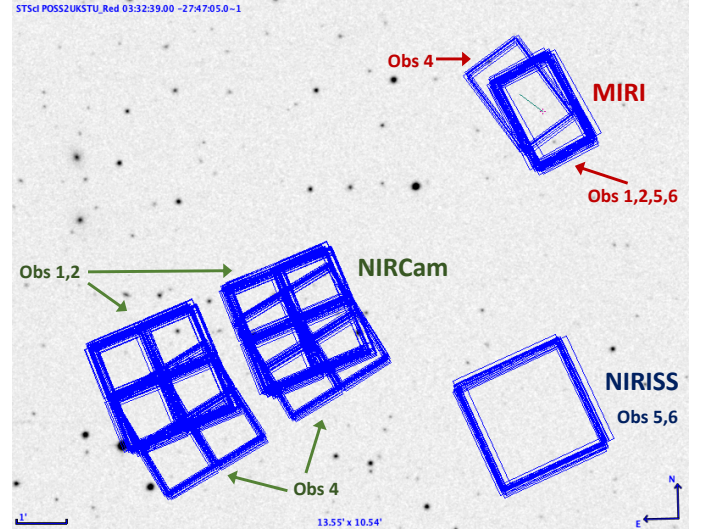

Fig. 1. Footprint of all observations obtained in GTO programme 1283 overlaid on DSS greyscale image (from APT/Aladin). To the upper right, the MIRI pointings for Observation 1, 2, 5, 6 (thicker rectangle) and 4 (rotated 10° anti-clockwise and offset ≈ 34″ towards the northeast) are shown. The Lyot region of the MIRI imager is not shown. The parallel fields for NIRISS (P3; Obs 5 and 6) and NIRCam (P2; Obs 1, 2 and 4) are indicated. Obs 4 was obtained at a different position angle due to JWST safing events making the schedule slip.
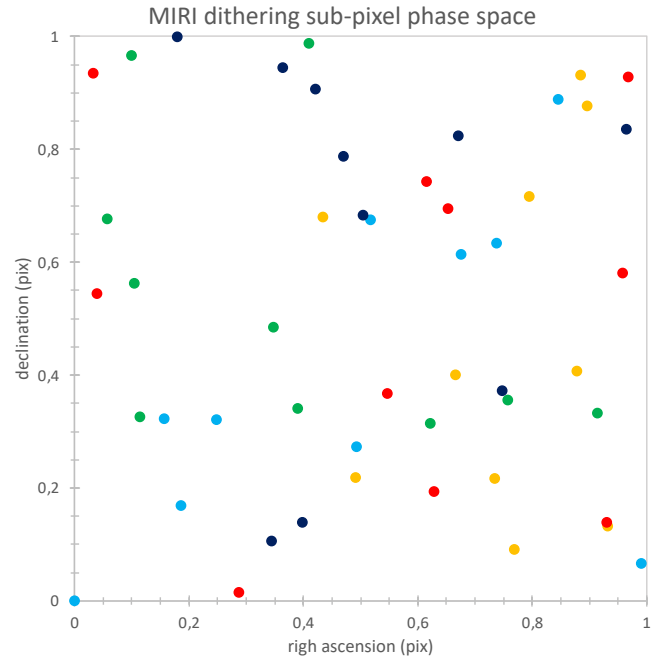

Fig. 2. MIRI imaging subpixel phase space sampling near detector centre, where the different colours refer to the different observations (1, 2, 4, 5, 6). The x axis shows $|\mathrm{frac}(x_i - x_1)|$ (i.e. the fractional pixel shift of the i'th dither position with respect to the 1st dither position in Obs 1) and the corresponding quantity on the y axis. The pixel scale for MIRI is 0.11″/pixel.

giving the most homogeneous background for our first internal release (v1.4), described below.

The adopted mosaic was reduced with the JWST pipeline version 1.12.3, pmap 1137, with several customised reduction steps especially developed for these data which we here describe (see
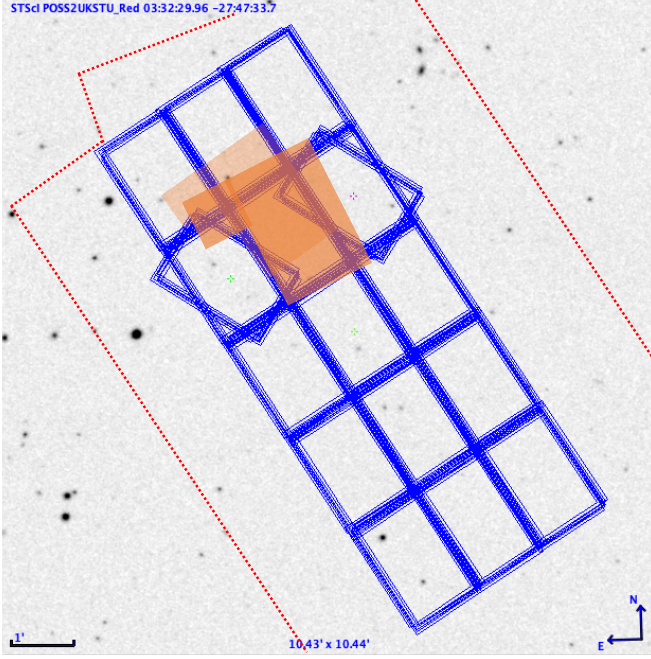
Fig. 3. Footprint of MIDIS MIRI imaging (orange shade) compared to the shallower SMILES survey area (blue). The dotted red lines outline the approximate border of the JADES NIRCam primary imaging field (Eisenstein et al. 2023a).

also Perez-Gonzalez et al. 2024a, and references therein): The MIRI F560W data present several artefacts that affect the homogeneity of the background, including a vertical (and a dimmer horizontal) striping (most prominent in the bottom quarter of the detector) and diffuse localised emission linked to cosmic ray showers. To cope with the former, after stage 1 and stage 2 of the JWST pipeline, a master super-background image was constructed for each one of the 96 exposures taken by MIDIS, using the median of the rest of the images obtained at different different dither positions to homogenise the background for a given exposure. The background patterns were found to be temporally variable, so we restricted the data to be used to correct a given exposure to images taken within a week. For the MIDIS dataset, this translated to completely independent super-background frames for the 2–6 December (Obs 1–2, 5–6) and 20 December (Obs 4) datasets. Before the median calculation, sources detected in an initial run of the JWST pipeline were masked in each individual exposure. This was done after correcting the WCS, which typically present $0.2''$–$0.6''$ offsets in the raw data compared to the final mosaics whose WCS is calibrated with Gaia star positions. Before producing the final superbackground image, all frames were homogenised to the same median background of the image that was corrected for background inhomogeneity. The effect of cosmic ray showers was partially taken into account by the JWST pipeline, but they are not totally corrected and this is still a significant contributor to the noise in the final mosaic. Our bespoke method also included a row and column median-filtering and a smooth (100×100 pixel^2) background subtraction to completely flatten the background accounting for very diffuse cosmic ray showers that are not handled by the pipeline. These additional processing steps applied to the JWST pipeline define our *customised* pipeline.

After the background was homogenised, we calibrated the WCS of each stage 2 image using the *tweakreg* external routine provided by the CEERS collaboration (Bagley et al. 2023),

using the Hubble Legacy Field catalogue (Whitaker et al. 2019) as the reference. Finally, all images were stacked using the JWST pipeline's stage 3.

The final output image was drizzled to different pixel scales: $0.11''$ (nominal MIRI pixel scale), $0.06''$ for robust MIRI only applications, and also $0.03''$ and $0.04''$ for various comparisons with NIRCam and HST data. For the finer pixel scale mosaics, we note that they may suffer from insufficient sampling in the external region. In Fig. 4 we show the resulting F560W image and the corresponding exposure map. Figure 5 shows a RGB composite with F560W in red, NIRCam/F356W in green, and F150W in blue, where the white contour outlines the limits of MIDIS (and outside of these limits the colours of galaxies appear blueish/greenish due to the missing red channel). In the same figure, the footprints of deep MUSE (blue, Bacon et al. 2023) and ALMA (red, for details see Boogaard et al. 2024) surveys are shown.

3.1. Noise measurements and pixel correlation

In order to determine the depth of the observations, we need to measure the background noise in our images on scales comparable to our detected sources. The noise levels are, in addition to the source size, affected by the photometric zeropoint and an aperture correction which in turn depends on the encircled energy distribution of the PSF.

In Fig. 6, we show how the background sky noise, measured on blank sky in $0.45''$ diameter apertures, scales with exposure time for our superbackground calibration (customised pipeline) and the nominal JWST pipeline output, showing the former to scale as $\sim 0.43/\sqrt{t}$, (where t is the exposure time), while the latter shows a much more modest decrease in the sky noise with t. This figure illustrates the improvement in background noise for our data customised pipeline reduction compared to the nominal JWST one.

The sub-pixel dithering and resampling in the drizzling procedure means that the output pixel fluxes become correlated, which artificially lowers the pixel-to-pixel RMS background noise in the output image (as it would in a box-car smoothing). These effects have been thoroughly discussed in Fruchter & Hook (2002); and as we have many dither positions uniformly filling the sub-pixel phase space (see Fig. 2), their equations 9 and 10 for calculating the scaling, R, with which the RMS should be multiplied, are expected to be directly applicable to our data.

We produced drizzled image mosaics of different scales ($s = s_{\text{out}}/s_{\text{in}}$, i.e. the output over nominal pixel scale) and *pixfrac* $p \in [1, 0.9, 0.7, 0.5, 0.0]$, enabling us to directly test the effect of pixel correlation on the background noise. For our nominal image mosaics with pixfrac $p = 1$, and scale $0.11''$ ($s = 1$, i.e. native scale), $0.06''$ ($s = 0.545$), $0.04''$ ($s = 0.36$), and $0.03''$ ($s = 0.27$), the noise correction factor that should be applied to the background noise is predicted to be $R = 1.5, 2.24, 3.13$ and 4.03, respectively.

There are different ways commonly employed to measure the background/sky noise in reduced images. For point sources (or quasi-point sources such as very faint galaxies), it is customary to perform aperture photometry, in an aperture with diameter d_{ap}. An aperture placed on blank sky will contain pixel values with a RMS of σ_{pix}. One can then take the average or median of the standard deviations measured in such apertures as $\langle \sigma_{\text{pix}} \rangle$; we here adopt the median, being more robust.

The 1σ sky noise, which we denote σ_{medpix} is then obtained by multiplying $\langle \sigma_{\text{pix}} \rangle$ with $\sqrt{N_{\text{pix}}}$ (where $N_{\text{pix}} = \pi(d_{\text{ap}}/2s_{\text{out}})^2$ is
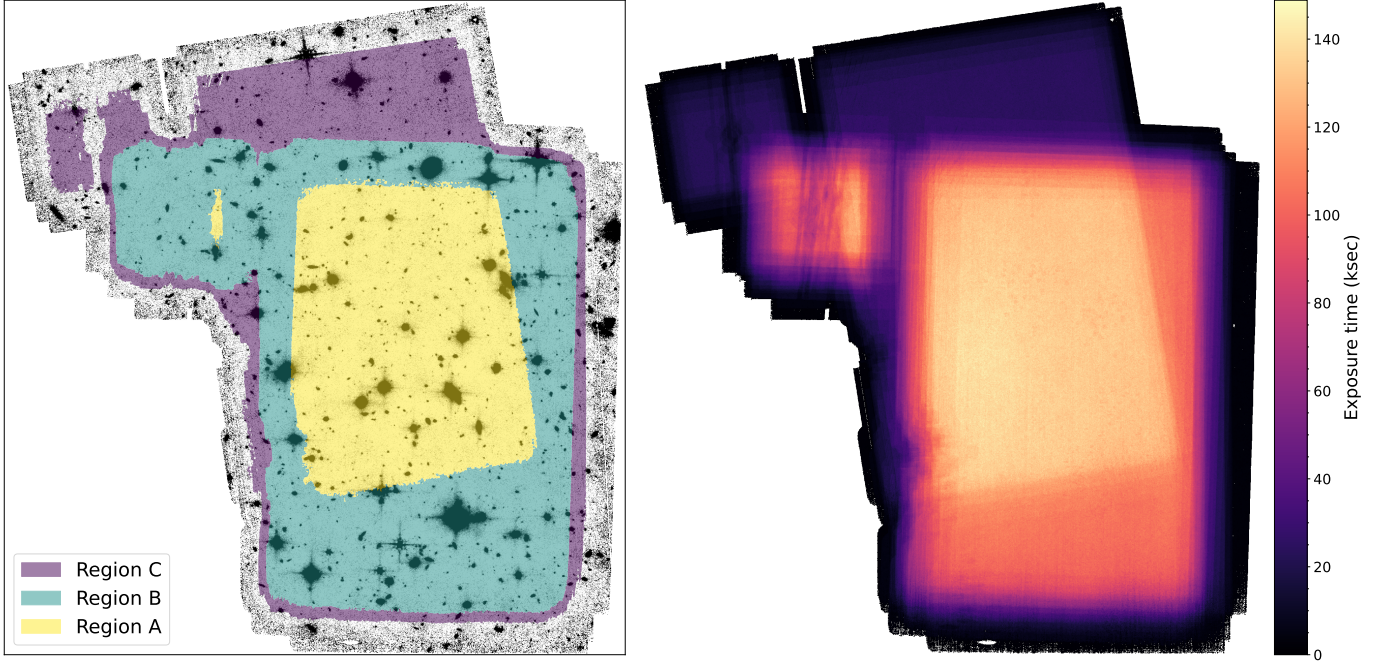
Fig. 4. Left: F560W image with linear intensity scaling. Coloured patches show regions with different depths where we have estimated the noise (see Table 1): the deepest area (A), where Obs 1–2, 4–6 overlap (yellow). The deep area (B), where Obs 4 does not overlap fully with the others (green). Outside these areas, there is coverage at less depth, notably the NE extension which only has observations from Obs 4. The area with at least 7h of combined integration is denoted C (purple). The orientation is in the detector plane (x,y). Right: Exposure time map.

the number of pixels in the aperture), and the correlation factor R above:

$$\sigma_{\mathrm{medpix}} = \langle\sigma_{\mathrm{pix}}\rangle \times \sqrt{N_{\mathrm{pix}}} \times R. \tag{1}$$

For this purpose, we first made a segmentation map, masking out regions with bright emission, and placed random apertures in the remaining area, while rejecting those that contain detected faint sources. We did this measurement in 1000 randomly drawn apertures for mosaics generated with different *pixfrac* applying the correction (R) for correlated noise, and arrived at close to identical estimates for $\langle\sigma_{\mathrm{pix}}\rangle$. Hence, the formulae of Fruchter & Hook (2002) accurately describes the effect of noise correlation when varying *pixfrac* in our dataset.

Another commonly used method, which to some extent mitigates the effect of pixel correlation, is to take the standard deviation ($\mathcal{S}$) of the total flux, f_{ap}, in apertures placed on blank sky close to an object:

$$\sigma_{\mathrm{aper}} = \mathcal{S}(f_{\mathrm{ap}}) \times R_{\mathrm{ap}}. \tag{2}$$

where R_{ap} accounts for the correlation between aperture fluxes (referred to as 'block sum' in Fruchter & Hook 2002, $R_{\mathrm{ap}} \ll R$). For a flat background of random noise, these two methods are identical. However, if the background is not perfectly flat over the image, σ_{aper} will be inflated. This does not affect the σ_{medpix} method because that measure uses the median of local noise estimates.

In our final image (v1.4), the low spatial frequency variations of the background have been removed by the superbackground subtraction, but our tests show that σ_{aper} is lower when measured semi locally (over regions smaller than $10'' \times 10''$) than globally by $\sim 30\%$, while σ_{medpix} remains constant, showing that the background subtraction, as expected, is not perfect and that small/medium spatial scale variations remain. However, when looking at the standard deviation of all pixels within the sky

apertures (defined as σ_{pix}) we find a sky noise which is constant with aperture size and much closer to the σ_{medpix} estimate. This reflects that the background variation on pixel to pixel scales is not very strong (but still causing the slightly higher noise level). The agreement between σ_{pix} and σ_{medpix} is good for $d_{\mathrm{ap}} = 0.45''$, with the former being marginally larger which we attribute to the remaining small scale background variation. In Fig. 7 we compare the noise measurements described above. The right-hand panel shows that the sky noise (here per pixel) is roughly constant with aperture size, except for σ_{aper}.

We finally compared our noise measurements to those provided by the error extension from the pipeline and found that the latter generally underestimates the true background noise[1]. The difference is smallest (and negligible) when employing $s = 1$ and $p = 0$, but increases for smaller pixel scales (s) and $p > 0$. We estimate the error extension noise (σ_{ERR}) by measuring the average variance inside the sky apertures.

For the case $s < 1, p > 0$ we find that the ratio $R_{\mathrm{err}} = \sigma_{\mathrm{medpix}}/\sigma_{\mathrm{ERR}}$ by which the error frame underestimates the noise increases with the aperture size, but is largely constant for $r_{\mathrm{ap}} \geq 0.225$ (i.e. $\sim$ two native MIRI pixels) and amounts to $R_{\mathrm{err}} = 1.72$ for $0.06''$ ($s = 0.545, p = 1$) and $R_{\mathrm{err}} = 2.5$ for $0.04''$ ($s = 0.36, p = 1$). Given that $1 < R_{\mathrm{err}} < R$, we conclude that the error frames from the JWST pipeline (version 1.12.3) to some extent but not fully account for the pixel correlation introduced by subpixel dithering and drizzling in MIRI, and should not be taken at face value.

---

[1] We note that the effects of our custom scripts added to the JWST pipeline have not been fully propagated into the error extension. Since the JWST pipeline gives larger background noise, the error extension would underestimate the true error even more.
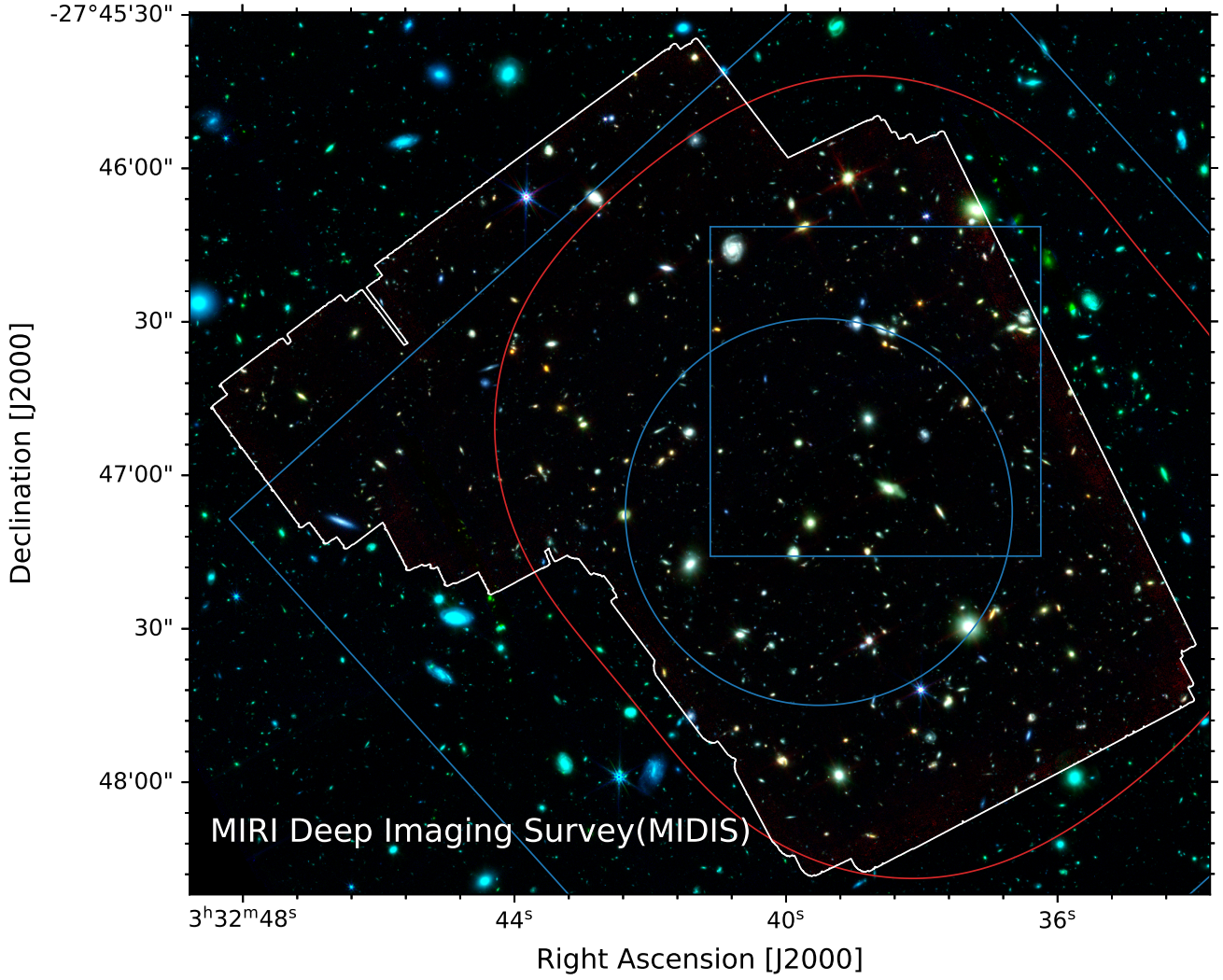
Fig. 5. RGB composite of the MIDIS field, with its boundaries outlined by the white contours (the irregular shape of the field is due to the use of two different pointings/PAs and that the nominal FOV has an extra square at the top left where the Lyot coronograph is located). The F560W filter is shown in red, NIRCam F356W in green, and F150W in blue (the latter two from JADES, Rieke et al. 2023). We note that the sources outside the white contour appear blueish/greenish due to the lack of MIRI data there. The thin blue contours outline deep MUSE spectroscopic surveys at 10 h and 30 h (large and small squares) and the MUSE eXtreme Deep Field (MXDF, circle) reaching up to 140 h (Bacon et al. 2023), and the red contour outlines the extent of the deep ALMA data from ASPECS at 1.2 mm and 3 mm (see Boogaard et al. 2024 for details).

3.2. Photometric depth

For the output mosaic with pixel scale $0.06''$ the measured 5σ average sky noise for $d_{ap} = 0.45''$ and using the σ_{medpix} method is 29.33 mag (1σ is 31.08 mag) in the deepest area (A). For a point source in a $d_{ap} = 0.45''$ aperture, the encircled energy fraction is 0.53, and hence our sky noise corresponds to a 5σ limiting point source magnitude of 28.65. However, given the large variations in the exposure time, we provide in Table 1 also the depth for areas B (28.5 mag) and C (27.7 mag) and the combined A+B area (28.6 mag). For the external area, the net exposure times vary even more, introducing larger variations in depth, but 27 mag can be taken as a representative value for the 5σ point source limit (see Table 1).

In Fig. 8, we show the variation in RMS sky noise (left) and resulting point source limiting magnitude (right). In making these maps, regions with sources have been interpolated over.

Our resulting point source depths can be compared to the prediction from the exposure time calculator which currently

gives 28.31 mag for a 40 h exposure (relevant for area A) in low background conditions (and with background measured in a $r = 0.5''-1.5''$ annulus). Hence, we are out-performing the ETC by ~0.35 mag. Improvements in the measured vs predicted depth of MIRI was found also in the SMILES survey (Alberts et al. 2014). Currently, the understanding and correction of cosmic ray showers is still developing[2,3]. It is not unlikely that a future improved handling of the cosmic ray showers could improve the depth of the MIRI Deep Survey even further.

Finally, we note that the background noise and point source limiting magnitudes also depend on the pixel scale adopted. The above measurements are for $0.06''$ and the same values are found

---

[2] https://jwst-docs.stsci.edu/known-issues-with-jwst-data/shower-and-snowball-artifacts#ShowerandSnowball Artifacts-showersShowers

[3] https://www.stsci.edu/files/live/sites/www/files/home/jwst/documentation/technical-documents/_documents/JWST-STScI-008545.pdf
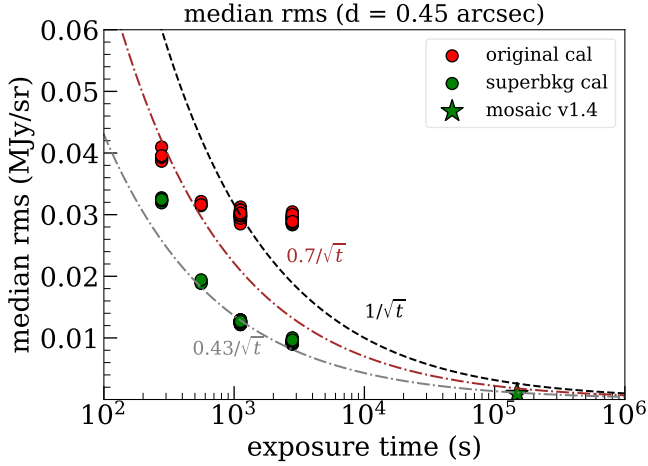
Fig. 6. Sky noise vs exposure time for the JWST pipeline output (red) and our customised pipeline including a super-background calibration (green). We stress that these have not been corrected for correlated noise induced by the drizzling procedure. The curves show different scalings of the RMS vs exposure time, but are not fits to the data.

for 0.11″ (native MIRI pixel scale), while for the 0.04″ and 0.03″ scales, the images are ∼0.05 magnitudes shallower.

4. Ancillary data

For a characterisation of the sources we make use of ancillary data of the HUDF/XDF area from HST (Illingworth et al. 2013), JWST: JEMS (Williams et al. 2004), FRESCO (Oesch et al. 2023) and JADES (Rieke et al. 2023). In addition we made use of published Spitzer/IRAC3 photometry (Stefanon et al. 2021). We also made use of the DAWN JWST Archive (DJA[4]) that coherently reduces, process and combines all public JWST observations using the GRIZLI pipeline (Brammer 2024). To enable multi-wavelength, multi-instrument analysis, the DJA mosaics are drizzled to a pixel scale of 0.04″ and aligned to GAIA DR3 (Valentino et al. 2023; Gillman et al. 2023, 2024). In accompanying papers we do, in addition, compare the MIRI results to available data from X-rays (Gillman et al. 2025), ALMA (Boogaard et al. 2024) and MUSE (Iani et al. 2024). We note that Fig. 5 is zoomed in on MIDIS which is fully encompassed by the wider area JADES and Spitzer surveys of the region (see also Fig. 3).

5. Photometry and source extraction

We have performed source detection with `python/sep` (Barbary et al. 2016) and basic aperture photometry with `python/photutils` (Bradley et al. 2024). In addition we present model based photometry based on THE FARMER (Weaver et al. 2023), which incorporates the effect of a varying PSF full width at half maximum (FWHM) for different filters in HST, NIRCam and MIRI.

5.1. Source detection and basic photometry

Source detection in the nominal 60 mas F560W image was done using `sep` (Barbary et al. 2016), a python wrapper for Source Extractor (Bertin & Arnouts 1996). In Table 2 we give

---

[4] `https://dawn-cph.github.io/dja/`

the extraction parameters used for the catalogue presented in this paper. We used the error maps from the JWST pipeline (scaled by a factor 1.7 to account for the noise underestimate in these maps, see Section 3.1) multiplied by the `threshfloat` parameter as the pixel detection threshold. As a first control of the detection, we applied a a SNR limit of 2 (2σ, Δmag < 0.5) estimated within the source segment (from the detection segmentation map). With these parameters and SNR rejection we find 2571 sources. Given that this is a single filter detection a large number of the faint sources are expected to be spurious, even when filtering the image before detection. We thus manually inspected the sources, rejecting 170 sources that are obviously spurious (single hot pixels, cosmic ray artefacts, PSF features and some sources near the detector edges) and arrive at a final object list containing 2401 sources.

We estimated the number of spurious sources by running the same detection on an inverted F560W image and applying the same SNR rejection. We also adjusted the spurious detection rate for the manual inspection. The rate of spurious detections in our final catalogue is 24% (of 2571 sources), which is higher than expected given the SNR cut applied. Hence, in addition to the 170 manually rejected sources, there are likely ∼400 spurious sources remaining, many of which will be ≲5σ sources, and the number of true sources is likely ≈2000. However, in this first single band catalogue for the deep MIRI data we have elected to be liberal in including sources (both in setting the detection parameters and in the manual inspection). Care should therefore be taken when using this catalogue, and multiple filters (e.g. NIRCAM data or other MIRI filters) should be used for any further characterisation of the sources. It should be noted that if we apply a more aggressive SNR cut the spurious rate naturally goes down, at SNR > 10 the rate is 2%. Why the spurious detection rate is higher than expected is hard to explain but a likely explanation could be image defects that remain in the stacked image due to problems with outlier (in particular cosmic ray) rejection. As the JWST pipeline improves in future releases, it is likely that the number of spurious sources will decrease. In Perez-Gonzalez et al. (2024b) and Jermann et al. (in prep.) we describe methods (based on investigating and rejecting individual frames) that can be used to verify that interesting sources are real, even with single filter detection. We note that the number of F560W > 2σ sources with a counterpart in the JADES catalogue is 1879.

Photometry was obtained for the detected sources using `photutils` and two different apertures: (i) circular apertures with a radius of 0.2″, and (ii) Kron apertures (Kron 1980). While the Kron apertures provides an estimate of the total flux of the sources, the small circular apertures will show smaller statistical errors with the caveat that not all of the flux is included. We aperture correct the circular aperture photometry using our PSF model (Boogaard et al. 2024). In Fig. 9 we display the resulting Kron aperture photometry for MIDIS.

5.2. Farmer photometry

Multi-wavelength (MIRI, NIRCam and HST) photometry was derived for all sources detected in the 0.04″ v1.4 F560W image with THE FARMER software (Weaver et al. 2023). THE FARMER simultaneously models all detected sources using parametric models, allowing accurate deblending of crowded fields and multi-wavelength datasets with varying resolutions. We opt for the 0.04″ F560W image to match with the images available in the DAWN JWST Archive (see Sect. 4).
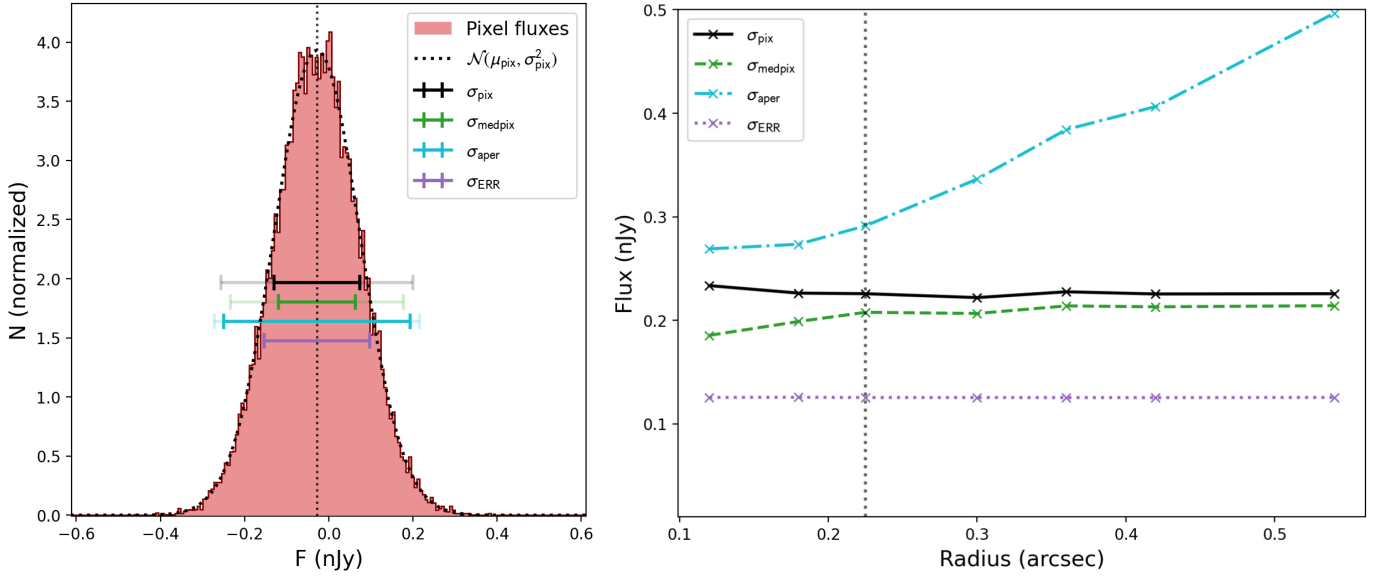
Fig. 7. Left panel: Flux distribution of all pixels within the sky apertures (see text). The distribution closely follows a normal distribution, show-casing that our method of selecting sky apertures is robust. The black error bar shows the observed standard deviation of the distribution, and the other bars show different noise estimates. The shaded extensions to the bars show the effect of applying the drizzle correlation factor (R and R_{ap}, for σ_{medpix}, and σ_{aper}, respectively). Comparing the extended green bar to the extended cyan bar then give very similar results. The black bar, gives the total statistics for all the pixels contained within our apertures. The purple bar shows the noise as inferred from the image error extension (σ_{ERR}). Right panel: The effect of aperture size on the noise estimates. We use an aperture radius of $0\overset{''}{.}225$ for the final noise estimate which is indicated by the vertical dashed black line. The noise estimates in this panel are all corrected for correlation (except for σ_{ERR}).

Table 1. Summary of noise and depth measurements.

Area id	Area $\square'$	Exp time (h)	σ_{medpix} (nJy/pix)	5σ limit (AB mag/nJy)
A	1.12	$\gtrsim 37$	0.20	28.65/12.6
B	1.64	$\gtrsim 24$	0.24	28.48/14.7
C	0.80	$\gtrsim 7$	0.50	27.68/30.8
A+B	2.76	$\gtrsim 24$	0.22	28.58/13.4
External	1.15	~ 1–6	~ 0.9	$\sim 27/\sim 50$

Notes. Areas are indicated in Fig. 4. σ_{medpix} calculated within apertures with diameter $\varnothing = 0.45''$, corrected for the drizzling correlation (a multiplicative factor 2.24, see text for details). The limiting magnitude is for a point source and includes the pixel correlation correction and aperture correction.

In brief, we first detected and modelled the galaxies in F560W MIRI band using our F560W PSF model (Boogaard et al. 2024). We then performed forced photometry in the other multi-wavelength bands, using the WEBBPSF models for NIRCam (Perrin et al. 2012, 2014), allowing for the flux to vary, whilst keeping the structural parameters fixed (details will be presented in Gillman et al., in prep.).

5.3. Comparison with Spitzer/IRAC

We have compared our F560W photometry to that of Spitzer/IRAC channel 3, which has a similar bandpass to F560W, for the HUDF (Guo et al. 2013; Stefanon et al. 2021). In Fig. 10 we show a comparison of our F560W photometry (measured with FARMER) and IRAC/Ch3. For fluxes $F \lesssim 10\,\mu$Jy we find very small flux differences consistent within the large photometric errors of the Spitzer/IRAC observations. At bright fluxes $F \gtrsim 20\,\mu$Jy, we see a gradual systematic brightening of

IRAC vs MIRI, amounting to $\gtrsim 20\%$ at the bright end. Either the Spitzer fluxes are too large, or the MIRI ones too small. The number of sources in the bright end is naturally small; nevertheless, we speculate on possible explanations for this offset in the next paragraph.

The Spitzer catalogue of Guo et al. (2013) contains matched photometry derived by determining the source position, size, and shape from the HST/F160W filter; matching the source shape to IRAC using the PSF, and finding the IRAC flux by fitting the convolved source model to the IRAC data. This is similar to the method used in FARMER, but for our photometry the morphology comes from the F560W image itself. In contrast, IRAC/Ch3 samples a factor of 3.5 longer wavelengths than the HST/F160W filter from which the source model was made. Most of the bright sources are at low ($z < 1$) redshift, meaning that HST/F160W samples $\lambda_{rest} \gtrsim 8000$ Å while IRAC/Ch3 samples $\lambda_{rest} \gtrsim 2.9\,\mu$m. If the size (e.g. the effective radius) or shape of the source varies with λ, this may give highly uncertain flux measurements, in particular for sources that are faint in the HST/F160W image, but bright in the mid-IR. In addition, for this redshift range, systematic offsets might be present if galaxies at a given brightness have consistently different morphologies between the rest-frame wavelengths probed by HST/F160W and IRAC/Ch3.

In addition to the FARMER photometry comparison we have also compared the IRAC measurements to photometry from *photutils* using large Kron apertures which show the same offset in the bright end. A more detailed investigation into this effect is outside the scope of this work, but we note that the MIRI/F560W photometry is obtained directly in high-resolution images and will thus give less model-dependent photometry.

We note that discrepant results for some bright sources were found also for JADES when comparing IRAC/Ch2 to F444W (Rieke et al. 2023), and in CEERS for MIRI/F560W and F770W (Yang et al. 2023), and for other MIRI/F560W fields (Sajkov et al. 2024). At least partly, this can be attributed to
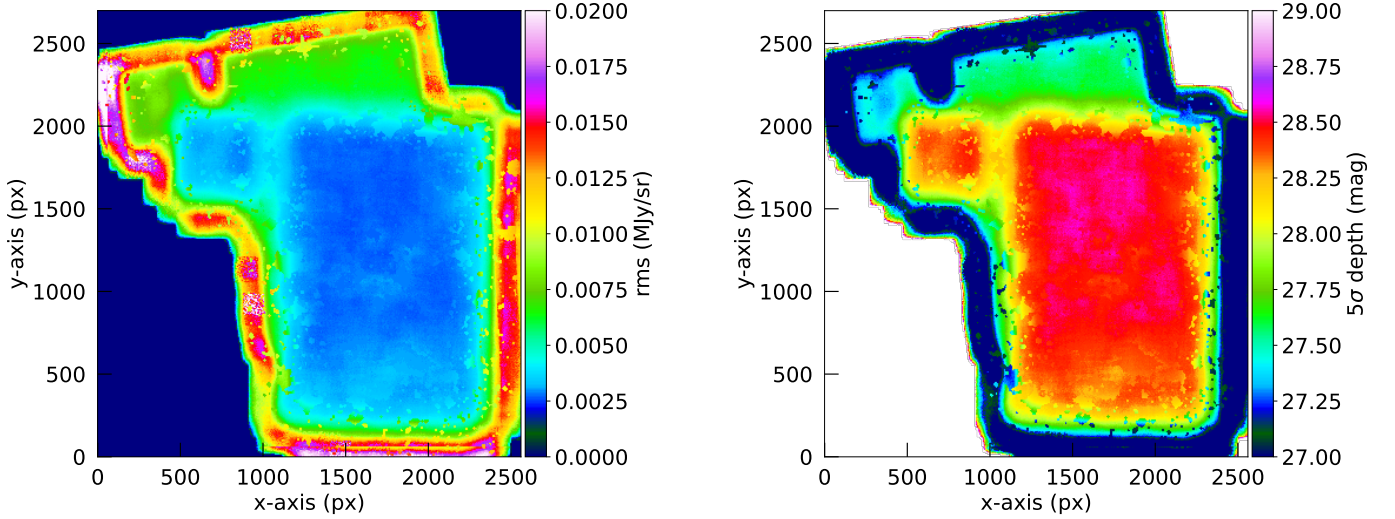
Fig. 8. RMS (left) and depth (right) map for output scale of 0.06″/pixel.

Table 2. Source detection parameters.

sep Parameter	Value
threshfloat	0.7
minarea	9
filter_kernel	Tophat with radius = 0.1″
clean_param	1.0
deblend_nthresh	128
deblend_cont	0.0001

source blending in the Spitzer data due to its order of magnitude broader PSF, an effect which is also present in the comparison for our data.

In Fig. 11, we show a comparison of our MIRI/F560W 5.6 μm image to the Spitzer/IRAC/Ch3 5.8 μm image (cropped to the size of the F560W image). The maximum depth of the Spitzer image is ∼40 hours reaching 25.6 mag (at 1σ, Stefanon et al. 2021, hence 5σ is ∼24 mag). The increase in resolution (a factor of ∼15) and depth (close to 5 magnitudes) despite the same exposure time is quite apparent.

6. Photometric redshifts

Photometric redshifts were derived from the multi-wavelength FARMER fluxes for each source using the EAZY software (Brammer et al. 2008). We used thirteen templates from the Flexible Stellar Populations Synthesis code (FSPS; Conroy & Gunn 2010) described in Kokorev et al. (2022) linearly combined to allow for maximum flexibility. The included spectroscopic redshifts are from the literature: the MUSE Hubble Ultra Deep Survey (Bacon et al. 2023), 3DHST (Brammer et al. 2012; Momcheva et al. 2016), and the JWST Advanced Deep Extragalactic Survey (JADES: Bunker et al. 2024; D'Eugenio et al. 2024).

While spectroscopic redshifts have been obtained for many galaxies in the XDF, both before and with JWST, photometric redshifts provide a more complete picture of the z-distribution, and to fainter flux levels. Photometric redshifts based on NIR-Cam photometry alone are expected to be quite secure, especially for star-forming systems based on the good coverage of
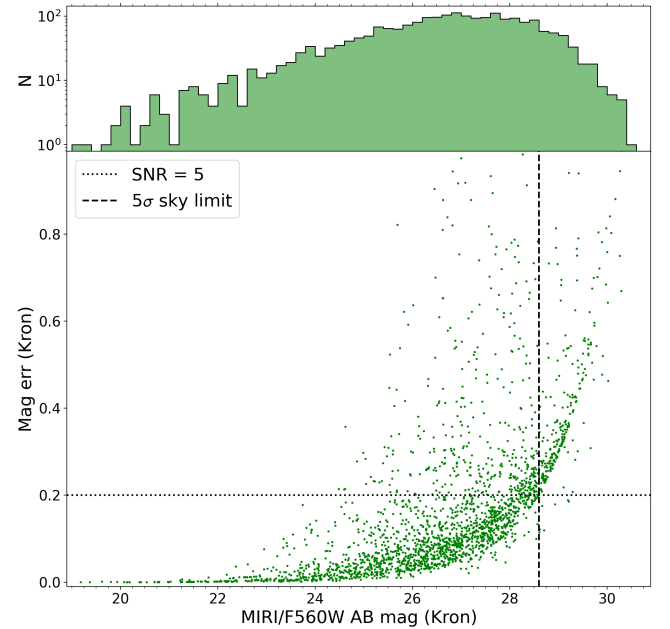
Fig. 9. Top: F560W number counts for Kron magnitudes. Bottom: F560W Kron magnitudes vs photometric uncertainty. The derived 5σ point source limiting magnitude is indicated by the dashed vertical line.

the rest frame UV and the Lyα break up to $z \gtrsim 10$. The power of MIRI is primarily to probe the rest frame optical and NIR for a more secure determination of the stellar population and identification of intrinsically red, for example dusty, sources. Nevertheless, it is interesting to investigate how the addition of MIRI affects the photo-z solution.

From the results of EAZY we analysed the systematic offsets between the observed and fitted SED to find a suggested zeropoint (ZP) error of $\Delta_{ZP} = -0.0388$. This is smaller than the median absolute offset for both NIRCam and HST filters. Hence, the MIRI calibration is from this comparison fully consistent with that of NIRCam, and suggests that the MIRI zero point is accurate. Moreover, we see no dependence of Δ_{ZP} for F560W with source brightness, suggesting that the offsets with respect to IRAC/Ch3 likely is due to the IRAC photometry rather than MIRI.
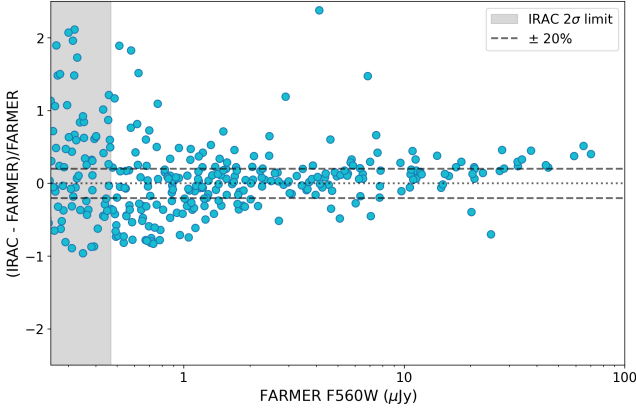
Fig. 10. Comparison of MIRI/F560W to IRAC/Ch3 photometry. For $<15\,\mu$Jy the fluxes agree, while for $>20\,\mu$Jy the IRAC photometry is systematically brighter.

In Fig. 12, we show the comparison of spectroscopic redshifts to photometric redshifts based on FARMER/EAZY. In total, we find 581 sources with spectroscopic redshifts and F560W photometric uncertainties better than 2σ within our field of view. We then define the redshift uncertainty as:

$$\sigma_z = \mathrm{Std}\left(\frac{z_{\mathrm{phot}} - z_{\mathrm{spec}}}{1 + z_{\mathrm{spec}}}\right) = \mathrm{Std}\,(\delta z),\qquad(3)$$

and classify all sources with $|\delta z| > 3\sigma_z$ as outliers (catastrophic failures). The fraction of catastrophic failures (shown as red circles in the figure) is 10% and the uncertainty for the remainder is $\sigma_z = 0.032$. Applying the same method to a comparison of the JADES (data release 2, Eisenstein et al. 2023b) photometric redshifts to the spectroscopic redshifts we find a similar uncertainty and catastrophic failure fraction. As expected the addition of F560W data does not improve the photometric redshift estimates over the full sample (but see Sect. 7.5).

In Fig. 13, we show the redshift distribution vs F560W magnitude. This figure includes, in addition to each source with a spectro-z (in red), photometric redshifts (in blue) for all galaxies (1069) for which the photo-z uncertainty $\Delta_z < 1$. Another $\sim$1000 sources have $\Delta_z > 1$, and have z_{ph} distributed from $\sim$0 to $\sim$18, with the majority at $z_{\mathrm{ph}} > 6$ and with peaks at $z \sim 0.6$, 4.5 and 12. While the individual redshifts of those are to be regarded as uncertain, a significant fraction is likely to be at $z > 6$. Finally, there are $\sim$500 sources with no phot-z solution at all from EAZY, many of which are likely to be spurious sources (see Section 5.1).

7. Results

The final MIRI image is shown in Fig. 5. As was described above, the photometric analysis shows that we reach a 5σ point source depth of 28.6 mag (AB), and that this is significantly deeper than the pre-launch and ETC estimates ($\sim$28.3). This demonstrates the spectacularly successful realisation of JWST (Gardner et al. 2023) and MIRI (Wright et al. 2023).

We show in Fig. 9 the resulting F560W magnitude distribution for the 2401 sources (but we note that there are likely spurious sources remaining, especially at $>$28 mag, see Sect.5.1). In Fig. 14 we show the F560W mag vs F356W–F560W colour for matched sources with $\geq 5\sigma$ in F560W and $\geq 2\sigma$ in F356W from JADES. For $1.5 < z < 10$, F560W probes the rest frame K-band (2.2 μm) to visual (0.5 μm) while NIRCam/F356W probes the

rest frame $\sim H$-band (1.6 μm) to the $\sim U$ band (0.32 μm). Hence this colour gives an indication of diversity of stellar populations present in the sample. Since sources are detected in both filters, and visually inspected, the spurious fraction should be very small, though likely not null.

7.1. Number counts

Fig. 9 (upper panel) shows the number of sources per 0.2 magnitude bin derived from the total MIRI image. The distribution peaks at $\sim$27 mag where it is rather flat and then turns down for $>$28 mag due to increasing incompleteness (varying over areas of different depth, see Fig. 4 and Table 1). Our peak counts at $\sim$27 mag are $\sim$90 mag^{-1} arcmin^{-2} ($3.4 \cdot 10^5$ per magnitude and $\square°$), which can be compared to Spitzer/Irac/Ch3 finding a factor of $\sim$15 lower surface density at $\sim$21 AB magnitudes (Fazio et al. 2004b, converted from a Vega magnitude of 17.3). Our counts at the same brightness suffer from low numbers given the small area of MIDIS but are at 4.8 ± 1.1 mag^{-1} arcmin^{-2} consistent with Spitzer finding 5.5 and 6.5 mag^{-1} arcmin^{-2} in two different fields.

For comparison, the F560W counts in CEERS (Yang et al. 2023) and SMILES (Stone et al. 2024) extend to $\sim$26 and $\sim$25.6 magnitudes, respectively. Deeper F560W counts were presented by Sajkov et al. (2024), based on 8 fields with exposure depth of 1.85 h per field, reaching $\sim$100% completeness at 0.1 μJy (26.4 mag) and a surface density for 0.09 μJy of $5.1 \pm 0.6 \cdot 10^5$ per square degree. This limit is brighter than what we get in the external area (outside of region C) where the 5σ photometric limit is typically $\gtrsim$27 or $>$0.05 μJy (see Fig. 8 and Table 2). Hence our total MIDIS area should be representative to 0.1 μJy at $\gtrsim 10\sigma$ with high completeness and with an insignificant number of spurious sources. We find (see Fig. 15) 856 sources down to 0.09 μJy, over a total area of 4.711 square arcmin or $6.54 \pm 0.22 \cdot 10^5$ per square degree (where the uncertainty quoted is the 1σ Poisson error), hence consistent within 2σ but suggesting that XDF is perhaps somewhat overdense at 5.6 μm. The total density of sources with F560W magnitude $\leq$27 (0.58 μJy, where we are reasonably complete over the full area) is $9.6 \cdot 10^5$ per square degree. Pushing the counts to fainter limits ($\lesssim$0.02 μJy) over areas A+B would require a more careful rejection of spurious sources which can be accomplished by including photometry from JADES and the upcoming deep F770W and F1000W imaging of XDF from JWST GO programme 6511.

7.2. Redshift distribution

As mentioned above, and shown in Fig. 12, for 90% of the 581 sources with F560W photometry above the 2σ level and available spectroscopic redshifts, the agreement with the photo-z derived from EAZY is very good ($\sigma_z \approx 0.03$, see Sect. 6 and Eq. (3)). In Fig. 13, we show the distribution of spectroscopic and photometric redshifts versus F560W magnitude. For the photo-z estimates we have only included sources with F560W fluxes $>2\sigma$ and and with a 1σ redshift uncertainty $\Delta_z < 1$, in total 1075 sources. While the selection functions for spectroscopic and photometric redshifts are different, they span a similar range, as shown in the histogram on top.

The bulk of MIRI/F560W sources with determined redshifts are at $z < 4$, but there is still a good number (74) of sources at $4 < z < 8$. For $z > 8$ the distribution thins out, with 3 objects at $z_{\mathrm{phot}} \sim 10-12$, among them JADES-GS-z11-0 (see Sect. 7.5). These sources all have F560W magnitudes close to 27. There is
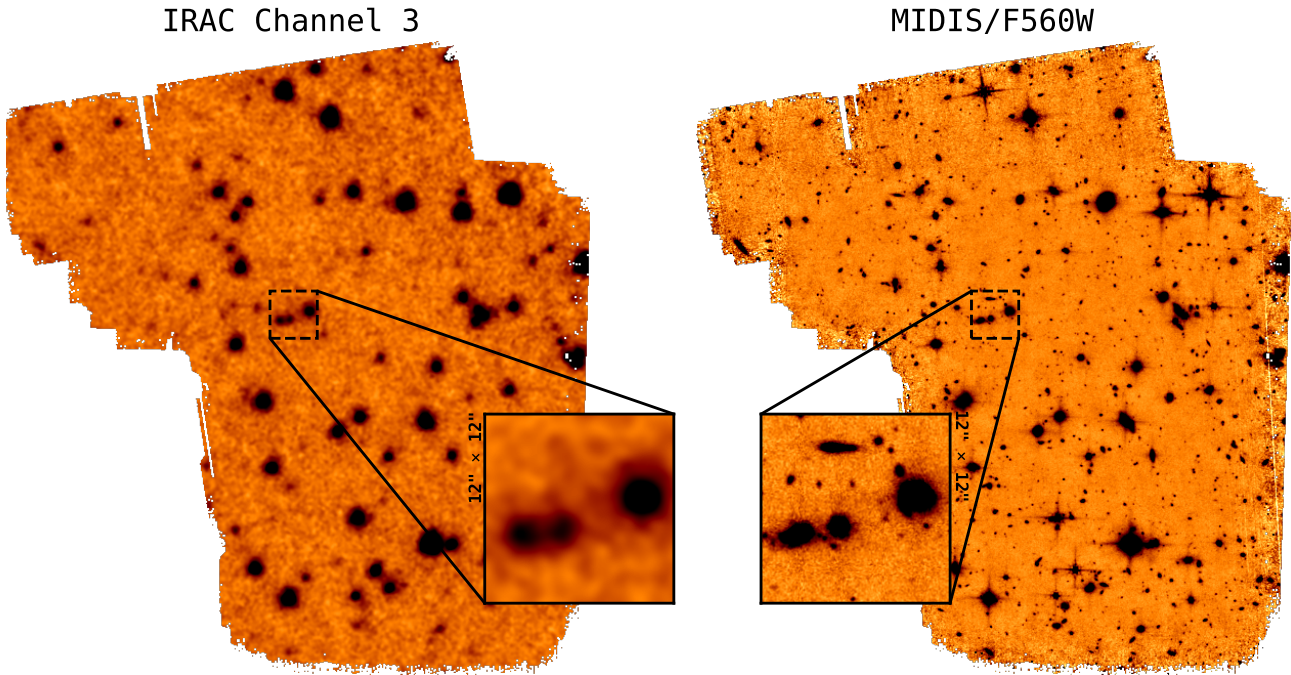
Fig. 11. Left: Spitzer/IRAC band 3 ($\lambda_{\rm eff}$ = 5.8 μm), based on exposure time of ~40 h, cropped to the size of the MIDIS field. Right: our MIRI/F560W image. The insets show a zoom-in on a 12″ × 12″ region highlighting the improvement in sensitivity and resolution.

a large number of fainter MIRI sources (up to 29th magnitude) with high-redshift ($z_{\rm phot}$ > 6) solutions but larger uncertainties (and the NIRCam photometric uncertainties are also larger for such, rendering the photo-z uncertainty being Δ_z > 1), and while uncertain a large fraction of these are expected to be at z > 6.

This demonstrates the ability of MIRI to detect galaxies in the EoR, at z > 6, but requires reaching depths of >27 magnitude in F560W. As NIRSPEC campaigns on the HUDF progress, an increased number of MIRI 5.6 μm sources with spectroscopic redshifts will likely emerge, and with deeper NIRCam images being obtained, also many fainter F560W sources will eventually get a reliable photo-z.

7.3. Morphologies

The FWHM of the MIRI PSF in F560W is 0.207″, corresponding to 1.4 kpc at z = 4. By tracing redder rest frame wavelengths ($\lambda_{\rm rest}$ > 1 μm at z < 4.6) than NIRCam, and with superior resolution and sensitivity compared to Spitzer and WISE, MIRI has a great potential for characterising the stellar mass distribution of high-redshift galaxies. In Fig. 16 we show an example of a galaxy at z = 2.454, also detected in CO and continuum with ALMA (Boogaard et al. 2024) with MIRI/F560W in red, NIRCam/F182M in green and HST/F814W in blue. Here, the MIRI emission (rest frame 1.6 μm) shown in red clearly traces an ellipsoidal shape indicative of an inclined disc, while the bluer filters (probing UV/visual) highlight (in yellow/green) smaller localised star-forming regions (for more galaxies and details, see Boogaard et al. 2024, where black/white single filter snapshots of individual galaxies also demonstrate this).

Several studies utilising the power of MIDIS to unveil the morphology of high-redshift galaxies are underway (Costantin et al. 2024; Gillman et al., in prep.; Moutard et al., in prep.). Another example is a study of X-ray detected AGN candidates (Gillman et al. 2025).

7.4. MIRI red sources

As can be seen from Fig. 14 most sources form a broad sequence of F356W–F560W ≈ −0.15±0.6, but there are also >100 sources with much redder colours, >1. We find in addition a similar number of red sources with upper (1σ) limits in F356W, which are in most cases previously unknown (i.e. not catalogued in JADES). Given that the F560W image still likely contains a significant number of spurious detections, sources with upper limits in F356W are not included in Fig. 14 and we do not discuss them further here. Sources with detections in both F560W and F356W are more secure.

We characterise the expected F356W–F560W colours of stellar populations of various age at different redshifts with the Yggdrasil spectral synthesis model[5] (Zackrisson et al. 2011) using an instantaneous burst model with metallicity Z = 0.004 and Kroupa initial mass function. We find that unreddened stellar populations with age < 1 Gyr would for z ≤ 10 not be expected to show F560W–F356W colours larger than 1.4, and for young populations (age ≤ 30 Myr) colours of <0.1 for z < 5 and <0.5 for z ≤ 10 are expected. At z = 3 an extinction of A_V = 5 would add 1.4 magnitude in colour; and at z = 8, A_V = 2 would add 1 magnitude in colour (assuming the attenuation law of Calzetti et al. 2000). Hence a source with F356W–F560W > 1.5 could either be a high-z quenched galaxy (with a predominantly old population), or a young (starburst) significantly reddened source with A_V > 5 at z ~ 3 or A_V > 2 at z ~ 8. We term such objects 'MIRI extremely red object' (MEROs). We note that already F356W–F560W > 1 would require A_V > 3 for a ≤30 Myr stellar population at z = 3 and A_V > 1 for z = 8; or alternatively a >300 Myr old population at z > 8, and such objects are termed 'MIRI red objects' (MROs). These colour criteria do not consider Galactic brown dwarf stars, which are rare but can have very red colours (Langeroodi & Hjorth 2023), or AGN. Of
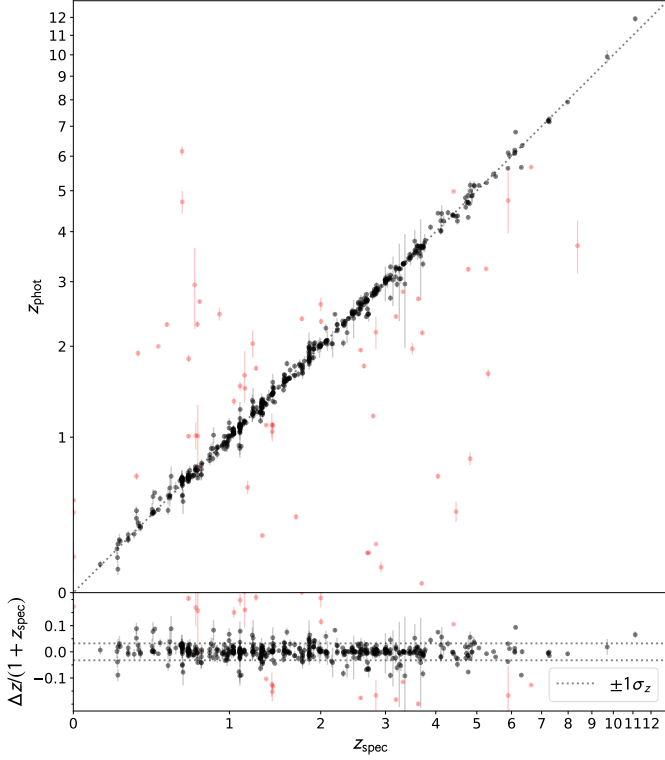
---

[5] https://www.astro.uu.se/~ez/yggdrasil/yggdrasil.html

Fig. 12. Upper panel: Photometric vs spectroscopic redshifts from the FARMER photometry and the EAZY code. The red points are outliers ($>3\sigma_z$). Lower panel: Normalised difference of the redshifts (with $\Delta z = z_{phot} - z_{spec}$) vs spectroscopic redshift. The standard deviation of the normalised difference is $\sigma_z = 0.032$ with the outliers removed.
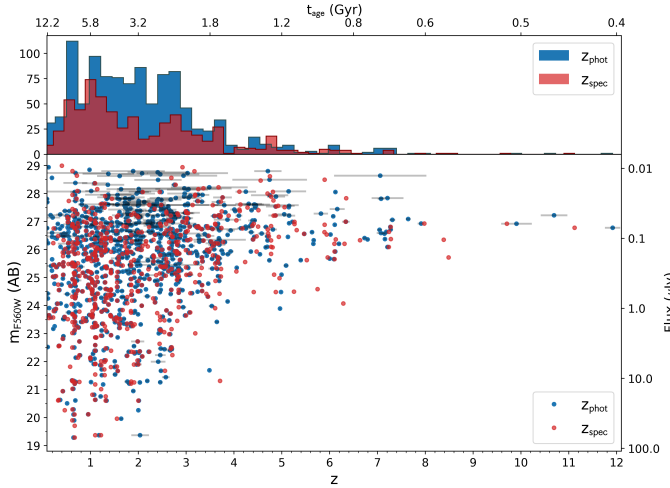

Fig. 13. Top: Histogram showing spectroscopic (red) and photometric (blue) redshift distribution. Bottom: Spectroscopic (red) and photometric (blue) redshift vs F560W magnitude. The photometric redshifts are estimated with EAZY. Only sources detected at $\sigma > 2$ in F560W, and with a 1σ redshift uncertainty $\Delta_z < 1$ were included (1069 sources).

relevance for the latter class, JWST has discovered a population of red compact sources (e.g. Barro et al. 2024), termed *little red dots*, many of which have broad Hα line emission (Matthee et al. 2024), and red NIRCam–MIRI colours (Perez-Gonzalez et al. 2024a), and likely represent a mix of dusty AGN and dusty starbursts.
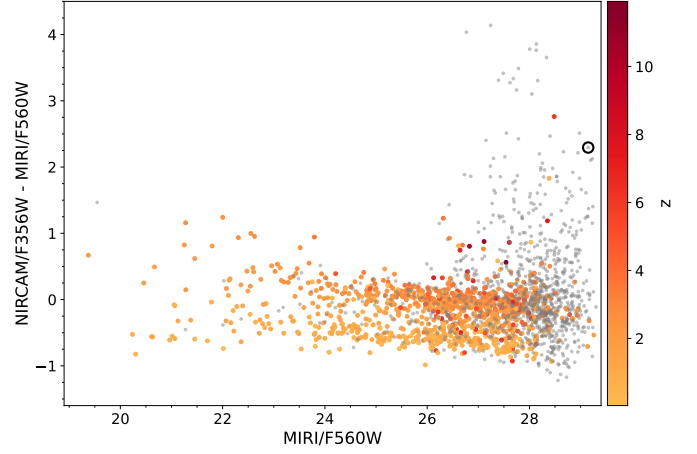
Fig. 14. F560W magnitude vs NIRCAM/F356W–F560W colour. Only sources with a F560W (F356W) magnitude uncertainty of 0.2 (0.5) or lower are included. The black circle indicates a confirmed MERO currently under investigation (Jermann et al., in prep.). The yellow–to–red colour scale indicate photometric redshift of the sources (grey, smaller, points do not have a valid redshift estimate).
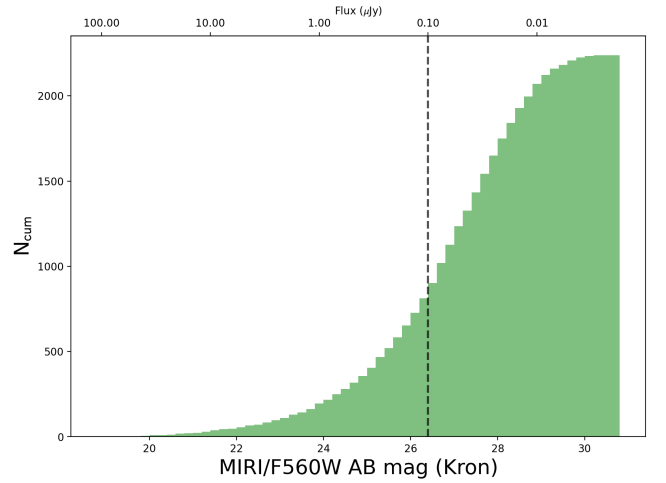
Fig. 15. F560W cumulative number counts for Kron magnitudes. The vertical dashed line indicates a flux limit of 0.10 μJy as in Sajkov et al. (2024).

As is evident from Fig. 14, out of the ~60 MERO candidates identifiable, only 2 sources currently have reliable photometric redshift estimates. For the similar number of MROs (with $1 <$ F356W–F560W < 1.5) five sources have photo-z estimates. However, most of the very red objects are also faint in F560W (~28 ± 1.3 mag). Given the complicated nature of cosmic ray residuals in the MIRI image (see Section 5.1) we still suspect that some of these objects could be spurious (also considering their low S/N in F356W). In order to confirm these objects as real astrophysical sources a more detailed procedure is needed. Such an investigation is currently underway and will be presented in Jermann at al. (in prep.), and one of the confirmed sources is indicated with a black circle in Fig. 14. Nevertheless, sources with F356W–F560W > 1 constitute a potential treasure trove for exploring dusty/old galaxies and AGN at high-z, but requires scrutiny in assessing their reality.

Naturally, the definition of MRO/MEROs according to the above reasoning depends on the filter combination used (for
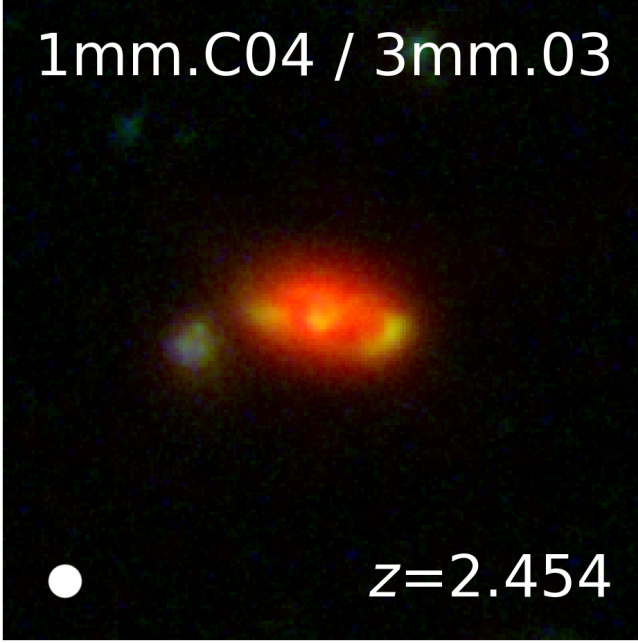
Fig. 16. Example of galaxy at cosmic noon ($z \sim 2.5$) as seen in MIRI/F560W (red), NIRCam/F182M (green) and HST/F814W (blue) from Boogaard et al. (2024). The MIRI emission unveils the presence of a disc-like stellar mass distribution, while the NIRCam and HST images highlight young star forming regions. The cutout is $4'' \times 4''$ (corresponding to $\sim 3 \times 3$ kpc). The FWHM ($0.207''$) of the MIRI/F560W PSF is shown as a white circle in the lower left.

instance, for F444W–F560W, the MRO criterion would be >0.5), and could be redefined for other colour indices, and in selecting sources for further study, all available photometric data should be used. Two examples of interesting MIRI red objects identified from other bands (F1000W) in MIDIS are the *Cerberus* source (Perez-Gonzalez et al. 2024b) detected at 2.8σ in F356W, and at 5.9σ F1000W (with F356W–F1000W = 4.1), but undetected in F560W (upper limit 29.7, implying F356W–F560W $\lesssim 1.5$); and the AGN candidate *Virgil* at $z = 6.6$ (Iani et al. 2023).

The cycle 3 JWST GO programme 6511 will image the XDF deeply with MIRI in F770W and F1000W. This will likely produce many more securely identified MIRI red objects.

7.5. High-redshift galaxies detected in MIDIS

In Fig. 17, we show photometric redshift fits of the eight highest redshift galaxies with a reliable photo-z estimate in our F560W selected catalogue. The fits are done with EAZY (see Section 6). We note that these are not bona fide SED fits, and use a limited grid for nebular emission, explaining why the strength of F560W (containing strong lines at these z) is not always well reproduced. The legend contains JADES id number, coordinates, JADES photo-z, our photo-z solution and its χ^2, and spectroscopic redshift (available for 4 of the sources). For all but one source (second row, right column) there is a good agreement between the photometric redshifts from JADES and our estimates. The discrepant source has a $z = 2.92$ solution in JADES (i.e. the drop in flux shortwards of 1.5 µm was identified as a Balmer break), but the bright F560W flux rule out this solution in favour of $z = 10.7$ where the F560W flux is boosted by $H\beta + [O\,III]$ emission. This illustrates the potential of MIRI for securing and characterising very high-redshift sources, pro-

vided faint flux levels can be reached. In Rinaldi et al. (2023) we used MIDIS F560W imaging to select 12 strong $H\alpha$ emitters at $z \approx 7-8$, and found them to have high ionising photon production efficiencies ($\xi_{\rm ion}$, see Rinaldi et al. 2024).

The XDF contains a number of EoR candidates known from past HST imaging studies (e.g. Oesch et al. 2013, including JADES-GS-z11-0 mentioned below). The field covered by our F560W image contains two spectroscopically confirmed $z > 10$ sources from JADES (Robertson et al. 2023; Curtis-Lake et al. 2023): JADES-GS-z10-0 and JADES-GS-z11-0. While the former is unfortunately contaminated by a F560W PSF spike preventing its secure detection, JADES-GS-z11-0 is well detected in F560W (see Fig. 17, lower left panel, but we note that the spectroscopic redshift is somewhat lower than the displayed photo-z fit) for the first time probing the rest frame >4300 Å emission. Notably, the galaxy is extended and presents some structure in the form of a southern extension in F560W, of which there is a hint also in NIRCam images. The extension is treated as a separate source in the JADES catalogue and has a lower (but very uncertain) photometric redshift in that catalogue. This source has recently been proposed to be a companion to JADES-GS-z11-0 (Hainline et al. 2024). The implications from the MIRI imaging will be further discussed in a forthcoming paper (Melinder et al., in prep.).

8. Summary and conclusions

Based on the MIRI European consortium GTO programme 1283, we present MIDIS (the MIRI Deep Imaging Survey) of the Hubble Ultra Deep Field, the deepest 5.6 µm image of the Universe as yet with a total integration time of 41 hours. We have processed the data with the JWST pipeline augmented by bespoke adaptations (our customised pipeline). We summarise our results as follows:

– The deepest parts of the mosaic reach a point source 5σ limiting AB magnitude of 28.65 (12.7 nJy). This is ~ 0.35 magnitudes better than the JWST exposure time calculator predicts.

– We detect ~ 2500 sources down to 2σ. Most of these (1879 sources) have counterparts at shorter wavelengths from JWST/NIRCam and the JADES survey. Due to remaining issues with the cosmic ray rejection in the JWST pipeline, we expect ~ 2000 of the F560W sources to be bona fide distant galaxies.

– Comparing the F560W photometry to Spitzer/IRAC Channel 3 observations of the HUDF, we find good agreement but we note that for sources brighter than 20.6 mag (20 µJy), IRAC fluxes are $\sim 20\%$ higher.

– There are 581 sources in MIDIS with availble spectroscopic redshifts, and for 1069 sources we could determine accurate photometric redshits (uncertainty in $z < 1$). For 90% of the sources with available spectroscopic redshifts, the agreement with photometric redshifts is excellent ($\sim 3\%$).

– While the majority of sources with available spectroscopic or accurate photometric redshift are at $z < 4$, the redshift distribution extends to $z \sim 12$. Many of the sources with less accurate photomtric redshift estimates are likely to be at $z > 6$.

– Number counts reveal a total density of sources ≤ 27 magnitudes (~ 0.06 µJy) in F560W of $\sim 10^6$ per square degree. Comparing to available F560W counts down to 0.09 µJy in other fields, we find the source density in MIDIS to be $\sim 25\%$ higher.
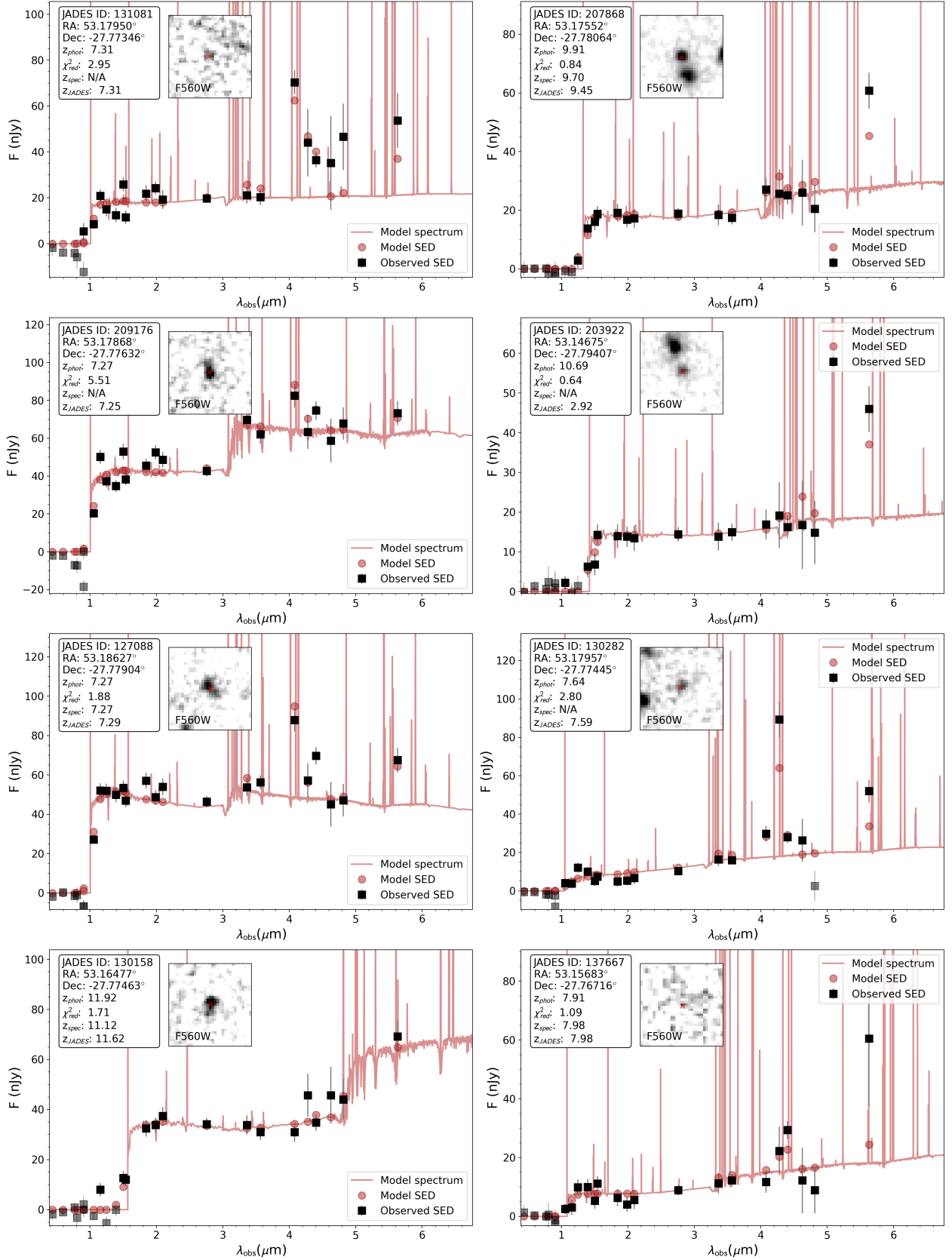
Fig. 17. Examples of photometric redshift fits made with EAZY for $\gtrsim 8$ galaxies in MIDIS. The insets show: (i) the source identification and redshift estimates; and (ii) F560W $2'' \times 2''$ thumbnails. The second (from top) panel on the right shows a source for which the addition of MIRI changed the photometric redshift solution from $z = 2.9$ to 10.7 due to the bright F560W flux being identified with Hβ + [O III].

- MIDIS imaging has been demonstrated to probe the NIR rest frame morphology of galaxies out to $z \sim 4$.
- More than 100 sources have F356W–F560W colours > 1 magnitude, representing MIRI very red sources, suggesting significant dust reddening or old stellar populations at high redshift.
- We illustrate the power of the MIDIS deep 5.6 μm survey by 8 examples of galaxies with $z_{\mathrm{phot}} > 7$, where in one case the MIRI F560W data point changes the redshift estimate from JADES from ~3 to >10.

Data availability

The catalogue data presented in this paper are available in electronic form at the CDS via anonymous ftp to cdsarc.cds.unistra.fr (130.79.128.5) or via https://cdsarc.cds.unistra.fr/viz-bin/cat/J/A+A/696/A57. Our F560W image mosaic is made available to the community. Although the data is publicly available in the archive, the image produced by the JWST pipeline version 1.12.3 (pmap 1137) is not yet as optimised as our current reduction (with a customised pipeline). We also make the F560W catalogue used for the results presented in this paper available as a machine readable table. The catalogue includes both standard photometric properties, and model based photometry from FARMER, see Table B.1 in Appendix B.

Our data products (images and catalogues) are available at MAST as a High Level Science Product via https://doi.org/10.17909/hfg7-8j02

When improvements in the JWST pipeline and calibrations so merit, updated images and an updated catalogue will be uploaded.

References

Alberts, S., Lyu, J., Shivaei, I., et al. 2014, ApJ, 976, 224
Bacon, R., Brinchmann, J., Conseil, S., et al. 2023, A&A, 670, A4
Bagley, M. B., Finkelstein, S. L., Koekemoer, A. M., et al. 2023, ApJ, 946, L12
Barbary, K., Boone, K., McCully, C., et al. 2016, https://doi.org/10.5281/zenodo.159035
Barro, G., Perez-Gonzalez, P. G., Kocevski, D. D., et al. 2024, ApJ, 963, 128
Becker, R. H., Fan, X., White, R. L., et al. 2001, AJ, 122, 2850
Beckwith, S. V. W., Stiavelli, M., & Koekemoer, A. M. 2016, AJ, 132, 1729
Bertin, E., & Arnouts, S. 1996, A&AS, 117, 393
Boogaard, L. A., Gilman, S., Melinder, J., et al. 2024, ApJ, 696, 27
Bosman, S. E. I., Davies, F. B., Becker, G. D., et al. 2022, MNRAS, 514, 55
Bosman, S. E. I., Álvarez-Márquez, J., Colina, L., et al. 2024, Nat. Astron., 8, 1054
Bouwens, R., Illingworth, G., Gonzalez, V., et al. 2010, ApJ, 725, 1587
Bouwens, R., Illingworth, G., Oesch, P., et al. 2015, ApJ, 803, 34
Bradley, L., Sipőcz, B., Robitaille, T., et al. 2024, https://doi.org/10.5281/zenodo.10967176
Brammer, G. 2024, https://doi.org/10.5281/zenodo.1146904
Brammer, G., van Dokkum, P., & Coppi, P. 2008, ApJ, 686, 1503
Brammer, G. B., van Dokkum, P. G., Franx, M., et al. 2012, ApJS, 200, 13
Bunker, A. J., Cameron, A. J., Curtis-Lake, E., et al. 2024, A&A, 690, A288
Calzetti, D., Armus, L., Bohlin, R. C., et al. 2000, ApJ, 533, 682
Caputi, K. I., Rinaldi, P., Iani, E., et al. 2024, ApJ, 969, 159
Casey, C. M., Kartaltepe, J. S., Drakos, N. E., et al. 2023, ApJ, 954, 31
Colina, L., Crespo, Gomez A., Alvarez-Marquez, J., et al. 2023, A&A, 673, L6
Conroy, C., & Gunn, J. E. 2010, Astrophysics Source Code Library [record ascl:1010.043]
Costantin, L., Gillman, S., Boogaard, L. A., et al. 2024, A&A, submitted [arXiv:2407.00153]
Covelo-Paz, A., Giovinazzo, E., Oesch, P. A., et al. 2025, A&A, 694, A178
Curtis-Lake, E., Carniani, S., Cameron, A., et al. 2023, Nat. Astron., 7, 622
D'Eugenio, F., Cameron, A. J., Scholtz, J., et al. 2024, ApJS, submitted [arXiv:2404.06531]
Dicken, D., Garcia, Marin M., Shivaei, I., et al. 2006, AJ, 132, 117
Eisenstein, D. J., Willot, C., Alberts, S., et al. 2023a, ApJS, submitted [arXiv:2306.02465]
Eisenstein, D. J., Johnson, B. D., Robertson, B., et al. 2023b, ApJS, submitted [arXiv:2310.12340]
Fan, X., Strauss, M. A., Becker, R. H., et al. 2006, AJ, 132, 117
Fazio, G. G., Hora, J. L., Allen, L. E., et al. 2004a, ApJS, 154, 10
Fazio, G. G., Ashby, M. L. N., Barmby, P., et al. 2004b, ApJS, 154, 39
Fruchter, A. S., & Hook, R. N. 2002, PASP, 114, 144
Gardner, J., Mather, J., Abbot, R., et al. 2023, PASP, 135, 8001
Giavalisco, M. 2002, ARA&A, 40, 579
Giavalisco, M., Ferguson, H. C., Koekemoer, A. M., et al. 2004, ApJ, 600, L93
Gillman, S., Gullberg, B., Brammer, G., et al. 2023, A&A, 676A, 26G
Gillman, S., Smail, I., Gullberg, B., et al. 2024, A&A, 691, A299
Gillman, S., Pye, J., Alonso-Herreri, A., et al. 2025, A&A, submitted [arXiv:2501.11491]
Gunn, J. E., & Peterson, B. A. 1965, ApJ, 142, 1633
Guo, Y., Ferguson, H. C., Giavalisco, M., et al. 2013, ApJS, 207, 23

Hainline, K. N., D'Eugenio, F., Jakobsen, P., et al. 2024, arXiv e-prints [arXiv:2404.04325]
Harikane, T., Ouchi, M., Oguri, M., et al. 2023, ApJS, 265, 5
Harikane, T., Nakajima, K., Ouchi, M., et al. 2024, ApJ, 960, 56
Hu, E. M., Cowie, L. L., & McMahon, R. G. 1998, ApJ, 502, L99
Iani, E., Rinaldi, P., Caputi, K. I., et al. 2023, ApJ, accepted [arXiv:2309.08515]
Iani, E., Caputi, K. I., Rinaldi, P., et al. 2024, ApJ, 963, 97
Illingworth, G. D., Magee, D., Oesch, P. A., et al. 2013, ApJS, 6, 13
Inoue, A. K., Shimizu, I., Iwata, I., & Tanaka, M. 2014, MNRAS, 442, 1805
Koekemoer, A. M., Faber, S. M., Ferguson, H. C., et al. 2011, ApJS, 197, 36
Kokorev, V., Brammer, G., Fujimoto, S., et al. 2022, ApJS, 263, 38
Kron, R. G. 1980, ApJS, 43, 305
Langeroodi, D., & Hjorth, J. 2023, ApJ, 957, L27
Lotz, J. M., Koekemoer, A. M., Coe, D., et al. 2017, ApJ, 837, 97
Lyu, J., Alberts, S., Rieke, G., & Rujopakarn, W. 2022, ApJ, 941, 191
Madau, P. 1995, ApJ, 441, 18
Matthee, J., Naidu, R. P., Brammer, G., et al. 2024, ApJ, 963, 129
Meyer, R. A., Oesch, P. A., Giovinazzo, E., et al. 2024, MNRAS, 535, 1067
Momcheva, I. G., Brammer, G. B., van Dokkum, P. G., et al. 2016, ApJS, 225, 27
Morrison, J., Dicken, D., Argyiou, I., et al. 2023, PASP, 135, 500
Oesch, P. A., Bouwens, R. J., Illingworth, G., et al. 2013, ApJ, 773, 75
Oesch, P. A., Brammer, G., Naidu, R. P., et al. 2023, MNRAS, 525, 2864
Papovich, C., Cole, J. W., Yang, G., et al. 2023, ApJ, 949, L18
Perez-Gonzalez, P. G., Costantin, L., Langeroodi, D., et al. 2023, ApJ, 951, L1
Perez-Gonzalez, P. G., Barro, G., Rieke, G. H., et al. 2024a, ApJ, 968, 4
Perez-Gonzalez, P. G., Rinaldi, P., Caputi, K. I., et al. 2024b, ApJ, 969, L10
Perrin, M., Soummer, R., Elliott, E. M., Lallo, M. D., & Sivaramakrishnan, A. 2012, SPIE Conf. Ser., 8442, 84423D
Perrin, M., Sivaramakrishnan, A., Lajoie, C.-P., Elliott, E. M., Pueyo, L., Ravindranath, S., & Albert, L. 2014, SPIE Conf. Ser., 9143, 91433X
Rieke, G., Wright, G., Böker, T., et al. 2015, PASP, 127, 584
Rieke, M. J., Robertson, B., Tacchella, S., et al. 2023, ApJS, 269, 16
Rieke, G., Alberts, S., Shivaei, I., et al. 2024, ApJ, 975, 83
Rigby, J., Perrin, M., McElwain, M., et al. 2023, PASP, 135, 8001
Rinaldi, P., Caputi, K. I., Costantin, L., et al. 2023, ApJ, 952, 143
Rinaldi, P., Caputi, K. I., Iani, E., et al. 2024, ApJ, 969, 12
Robertson, B., Tacchella, S., Johnson, B. D., et al. 2023, Nat. Astron., 7, 611
Sajkov, P., Sajina, A., Pope, A., et al. 2024, ApJ, 977, 115
Stefanon, M., Labbe, I., Oesch, P. A., et al. 2021, ApJS, 257, 68
Steidel, C., & Hamilton, D. 1992, AJ, 104, 941
Steidel, C., Giovalisco, M., Pettini, M., Dickinson, M., & Adelberger, K. 1996a, ApJ, 462, L17
Steidel, C., Giovalisco, M., Dickinson, M., & Adelberger, K. 1996b, AJ, 112, 352
Stone, M. A., Alberts, S., Rieke, G. H., et al. 2024, arXiv e-prints [arXiv:2405.18470]
Thompson, R. I., Storrie-Lombardi, L. J., Weymann, R. J., et al. 1999, AJ, 117, 17
Valentino, F., Brammer, G., Gould, K. M. L., et al. 2023, ApJ, 947, 20V
Weaver, J., Zalesky, L., Allen, N., & Taamoli, S. 2023, Astrophysics Source Code Library [record ascl:2312.016]
Whitaker, K. E., Ashas, M., Illingworth, G., et al. 2019, ApJS, 244, 16
Williams, R. 2018, Hubble Deep Field and the Distant Universe (Bristol, UK: IOP Publishing)
Williams, R. E., Blacker, B., Dickinson, M., et al. 1996, AJ, 112, 1335
Williams, R. E., Baum, S., Bergeron, L. E., et al. 2000, AJ, 120, 2735
Williams, C. C., Tacchella, S., Maseda, M. V., et al. 2004, ApJS, 268, 64
Wright, G., Wright, D., Goodson, G., et al. 2015, PASP, 127, 595
Wright, G., Rieke, G., Glasse, A., et al. 2023, PASP, 135, 8003
Yang, G., Papovich, C., Bagley, M. B., et al. 2023, ApJ, 956, L12
Zackrisson, E., Rydberg, C. E., Schaerer, D., Östlin, G., & Tuli, M. 2011, ApJ, 740, 13

[1] Department of Astronomy, Oskar Klein Centre, Stockholm University, AlbaNova University Center, 10691 Stockholm, Sweden
[2] Centro de Astrobiología (CAB), CSIC-INTA, Ctra. de Ajalvir km 4, Torrej'on de Ardoz 28850, Madrid, Spain
[3] DTU Space, Technical University of Denmark, Elektrovej 327, 2800 Kgs. Lyngby, Denmark
[4] Kapteyn Astronomical Institute, University of Groningen, PO Box 800, 9700 AV Groningen, The Netherlands
[5] Max-Planck-Institut für Astronomie, Königstuhl 17, 69117 Heidelberg, Germany
[6] Cosmic Dawn Centre (DAWN), Copenhagen, Denmark
[7] UK Astronomy Technology Centre, Royal Observatory Edinburgh, Blackford Hill, Edinburgh EH9 3HJ, UK
[8] Department of Physics and Astronomy, University College London, Gower Place, London WC1E 6BT, UK
[9] Institute for Theoretical Physics, Heidelberg University, Heidelberg, Germany
[10] I. Physikalisches Institut der Universität zu Köln, Zülpicher Str. 77, 50937 Köln, Germany
[11] European Space Agency, Space Telescope Science Institute, Baltimore, MD, USA
[12] DARK, Niels Bohr Institute, University of Copenhagen, Jagtvej 155A, 2200 Copenhagen, Denmark
[13] Aix Marseille Université, CNRS, LAM (Laboratoire d'Astrophysique de Marseille) UMR 7326, 13388 Marseille, France
[14] AURA for the European Space Agency (ESA), Space Telescope Science Institute, 3700 San Martin Drive, Baltimore, MD, USA
[15] Department of Astronomy, University of Geneva, Chemin Pegasi 51, 1290 Versoix, Switzerland
[16] European Space Agency (ESA), European Space Astronomy Centre (ESAC), Camino Bajo del Castillo s/n, 28692 Villaneuva de la Canada, Madrid, Spain
[17] School of Physics & Astronomy, Space Park Leicester, University of Leicester, 92 Corporation Road, Leicester LE4 5SP, UK
[18] Dublin Institute for Advanced Studies, Astronomy & Astrophysics Section, 31 Fitzwilliam Place, Dublin 2, Ireland
[19] Centre for Extragalactic Astronomy, Durham University, South Road, Durham DH1 3LE, UK
[20] Leiden Observatory, Leiden University, PO Box 9513, 2300 RA Leiden, The Netherlands
[21] University of Vienna, Department of Astrophysics, Türkenschanzstrasse 17, 1180 Vienna, Austria
[22] Institute of Particle Physics and Astrophysics, ETH Zürich, Wolfgang-Pauli-Str 27, 8093 Zurich, Switzerland
[23] AIM, CEA, CNRS, Université Paris-Saclay, Université Paris Diderot, Sorbonne Paris Cité, 91191 Gif-sur-Yvette, France
[24] Institute of Astronomy, KU Leuven, Celestijnenlaan 200D bus 2401, 3001 Leuven, Belgium
[25] Centro de Astrobiología (CAB), CSIC-INTA, Camino Bajo del Castillo s/n, E-28692 Villanueva de la Cañada, Madrid, Spain
[26] Telespazio UK for the European Space Agency (ESA), ESAC, Camino Bajo del Castillo s/n, 28692 Villanueva de la Cañada, Spain
[27] Steward Observatory, University of Arizona, 933 North Cherry Avenue, Tucson, AZ 85721, USA
[28] INAF – Osservatorio Astronomico di Padova, Vicolo dell'Osservatorio 5, Padova I-35122, Italy
[29] Institute of Science and Technology Austria (ISTA), Am Campus 1, 3400 Klosterneuburg, Austria
[30] Max-Planck-Institut für Radioastronomie (MPIfR), Auf dem Hügel 69, D-53121 Bonn, Germany

Appendix A: Table of observations

Table A.1. JWST observations for programme 1283

Obs id	PA (°)	dith pos	offset x,y (arcsec)	nexp	nint	totint	time (s)	date	parallel observation
1	27.8	1-10	0, 0	10	10	100	28 000.2	Dec 5, 2022	NIRCam/F115W/F277W
2	27.8	11-20	0.0275, 0.03663	10	10	100	28 000.2	Dec 6, 2022	NIRCam/F115W/F277W
4	36.8	31-40	10.03663, -32.96337	10	10	100	28 000.2	Dec 20, 2022	NIRCam/F150W/F356W
5	25.8	0	0, 0	1	1	1	277.5	Dec 2, 2022	NIRISS/F115W
		41-49		9	4	36	10 065.0		NIRISS/F115W/GR150R
		0		1	1	1	277.5		NIRISS/F115W
		0		1	1	1	277.5		NIRISS/F150W
		41-49		9	4	36	10 065.0		NIRISS/F150W/GR150R
		0		1	1	1	277.5		NIRISS/F150W
		0		1	2	2	557.8		NIRISS/F200W
		41-49		9	4	36	10 065.0		NIRISS/F200W/GR150R
		0		1	2	2	557.8		NIRISS/F200W
6	25.8	0	0.0328, 0.0328	1	1	1	277.5	Dec 3, 2022	NIRISS/F115W
		50-58		9	4	36	10 065.0		NIRISS/F115W/GR150C
		0		1	1	1	277.5		NIRISS/F115W
		0		1	1	1	277.5		NIRISS/F150W
		50-58		9	4	36	10 065.0		NIRISS/F150W/GR150C
		0		1	1	1	277.5		NIRISS/F150W
		0		1	2	2	557.8		NIRISS/F200W
		50-58		9	4	36	10 065.0		NIRISS/F200W/GR150C
		0		1	2	2	557.8		NIRISS/F200W
Sum				96		532	148 842		

Notes. 'PA' refers to the position angle of the MIRI field orientation. 'dith pos' correspond to the points in the MIRI-CYCLING-MEDIUM pattern, and 0 corresponds to the nominal position for no dither. 'Offset x,y' is with respect to the nominal position, applied by SPECIAL REQUIREMENT. 'nexp' refer to the number of dithered exposures, 'nint' the number of 100 groups integrations obtained at each dither position, and 'totint' the total number of 100 group integrations.

Appendix B: MIDIS catalogue format

Table B.1. MIDIS catalogue column description

Column	Name	unit	Content
1	MIDIS ID	...	...
2	JADES ID	...	Cross-referenced (see text)
3	RA	degree	ICRS Coordinate
4	DEC	degree	ICRS Coordinate
5	a	arcsec	semi-major axis
6	b	arcsec	semi-minor axis
7	THETA	degree	orientation on sky
8	e	...	ellipticity
9	Z_PHOT	...	Photometric redshift
10	Z_PHOT_ERR	...	Photometric redshift uncertainty[a]
11	Z_SPEC	...	Spectroscopic redshift
12	Z_SPEC_REF	...	Spectroscopic redshift reference[b]
13	FLUX_APER_F560W	nJy	Circular aperture flux F560W[c]
14	FLUXERR_APER_F560W	nJy	Circular aperture flux uncertainty F560W[c]
15	FLUX_KRON_F560W	nJy	Kron aperture flux F560W[d]
16	FLUXERR_KRON_F560W	nJy	Kron aperture flux uncertainty F560W[d]
17	MAG_APER_F560W	...	Circular aperture magnitude F560W
18	MAGERR_APER_F560W	...	Circular aperture magnitude uncertainty F560W
19	MAG_KRON_F560W	...	Kron aperture magnitude F560W
20	MAGERR_KRON_F560W	...	Kron aperture magnitude uncertainty F560W
21	FLUX_FARMER_F560W	nJy	Total flux from FARMER F560W
22	FLUXERR_FARMER_F560W	nJy	Total flux error from FARMER F560W
23	MAG_FARMER_F560W	...	Total magnitude from FARMER F560W
24	MAGERR_FARMER_F560W	...	Total magnitude error from FARMER F560W
25	FLUX_APER_F356W	nJy	Circular aperture flux F356W[c]
26	FLUXERR_APER_F356W	nJy	Circular aperture flux uncertainty F356W[c]
27	MAG_APER_F356W	...	Circular aperture magnitude F356W
28	MAGERR_APER_F356W	...	Circular aperture magnitude uncertainty F356W

Notes. This table contains descriptions of the columns available in the machine readable table. The catalogue data is avaiable at CDS. The catalogue contains all the measurements used in the figures presented. The JADES IDs given in the table correspond to the ID column in the JADES v2.0 photometric catalogue (Eisenstein et al. 2023b; D'Eugenio et al. 2024, DOI:10.17909/8tdj-8n28). We use the JADES v2.0 image for the F356W measurements (D'Eugenio et al. 2024). For an up to date catalogue (which also contains measurements in more NIRCAM filters) please refer to the MAST HLSP page for MIDIS (xxx). Morphological measurements are obtained in the F560W MIDIS image using the `photutils` Python package. All magnitudes are given in the AB system.
[a] Calculated as the 68% confidence interval from EAZY divided by two.
[b] Spectroscopic redshifts come from various sources. The following abbreviations are used in the table for the different references: B23 – Bacon et al. (2023), CP24 – Covelo-Paz et al. (2025), DE24 – D'Eugenio et al. (2024), M24 – Meyer et al. (2024).
[c] Fluxes are measured with circular apertures of radius 0.2″, aperture corrected using the JWST CRDS `apcor` file. Errors are estimated from a local pixel-to-pixel noise estimate corrected for the resampling correlation.
[d] Measured in elliptical Kron (Kron 1980) apertures as implemented by `photutils`. The default scaling parameters are used for the Kron aperture, but the minimum circular radius is set to 0.4″.